A large-scale volumetric correlated light and electron microscopy study localizes Alzheimer's disease-related molecules in the hippocampus

Xiaomeng Han[1], Peter H. Li[2], Shuohong Wang[1], Morgan Sanchez[3], Sneha Aggarwal[4], Tim Blakely[2], Richard Schalek[1], Yaron Meirovitch[1], Zudi Lin[5], Daniel Berger[1], Yuelong Wu[1], Fatima Aly[6], Sylvie Bay[7], Benoît Delatour[8], Pierre LaFaye[9], Hanspeter Pfister[5], Donglai Wei[4], Viren Jain[2], Hidde Ploegh[10], Jeff Lichtman[1*]

[1] Department of Molecular and Cellular Biology, Harvard University, Cambridge, MA

[2] Google Research, Mountain View, CA

[3] Department of Biomedical Informatics, Harvard Medical School, MA

[4] Computer Science Department, Boston College, Chestnut Hill, MA

[5] School of Engineering and Applied Sciences, Harvard University, Cambridge, MA

[6] Harvard College, MA

[7] Institut Pasteur, Université Paris Cité, CNRS UMR 3523, Unité de Chimie des Biomolécules; Paris, France

[8] Paris Brain Institute (ICM), CNRS UMR 7225, INSERM U1127, Sorbonne Université, Hôpital de la Pitié-Salpêtrière; Paris, France

[9] Institut Pasteur, Université Paris Cité, CNRS UMR 3528, Antibody Engineering Platform; Paris, France

[10] Program of Cellular and Molecular Medicine, Boston Children's Hospital, Boston, MA

[*] Corresponding Author: jeff@mcb.harvard.edu

Abstract

Connectomics is a nascent neuroscience field to map and analyze neuronal networks. It provides a new way to investigate abnormalities in brain tissue, including in models of Alzheimer's disease (AD). This age-related disease is associated with alterations in amyloid-β (Aβ) and phosphorylated tau (pTau). These alterations correlate with AD's clinical manifestations, but causal links remain unclear. Therefore, studying these molecular alterations within the context of the local neuronal and glial milieu may provide insight into disease mechanisms. Volume electron microscopy (vEM) is an ideal tool for performing connectomics studies at the ultrastructural level, but localizing specific biomolecules within large-volume vEM data has been challenging. Here we report a volumetric correlated light and electron microscopy (vCLEM) approach using fluorescent nanobodies as immuno-probes to localize Alzheimer's disease-related molecules in a large vEM volume. Three molecules (pTau, Aβ, and a marker for activated microglia (CD11b)) were labeled without the need for detergents by three nanobody probes in a sample of the hippocampus of the 3xTg Alzheimer's disease model mouse. Confocal microscopy followed by vEM imaging of the same sample allowed for registration of the location of the molecules within the volume. This dataset revealed several ultrastructural abnormalities regarding the localizations of Aβ and pTau in novel locations. For example, two pTau-positive post-synaptic spine-like protrusions innervated by axon terminals were found projecting from the axon initial segment of a pyramidal cell. Three pyramidal neurons with intracellular Aβ or pTau were 3D reconstructed. Automatic synapse detection, which is necessary for connectomics analysis, revealed the changes in density and volume of synapses at different distances from an Aβ plaque. This vCLEM approach is useful to uncover molecular alterations within large-scale volume electron microscopy data, opening a new connectomics pathway to study Alzheimer's disease and other types of dementia.

Keywords

Aβ40/42, hyperphosphorylated tau, CD11b, microglia, nanobody, hippocampus CA1, ultrastructure, synapse, volume electron microscopy, serial section electron microscopy, connectomics

Introduction

Connectomics is a branch of neuroscience that uses high-throughput computer-assisted imaging and analysis to structurally map complete neuronal networks in selected organisms (Lichtman & Sanes, 2008). The hope is that this analysis will ultimately provide insights into how neural circuits function or malfunction in healthy or diseased human brains. This approach is already being used in human tissue (Loomba et al., 2022; Shapson-Coe et al., 2021). A recent human connectomic dataset acquired with automated image acquisition and machine learning segmentation of a 1 mm^3 volume of cortex provided the structure and connectivity of 20,000 neurons and 160 million synapses (Shapson-Coe et al., 2021). Because the cognitive impairments of Alzheimer's disease (AD) are related to abnormalities in neural networks (Yu et al., 2021), connectomics may also provide a pathway to study this disorder within the detailed context of neuronal connectivity at the level of individual synapses.

Electron microscopy is a powerful modality to map the ultrastructure of synaptic connections owing to its nanometer level resolution and the non-specific staining of lipid bilayers by heavy metals (Hayat, 2000). Early studies using transmission electron microscopy (TEM) on single ultrathin sections of samples obtained from patients with Alzheimer's disease showed a decline of synapse density (DeKosky & Scheff, 1990; S. W. Scheff et al., 1990; S. W. Scheff & Price, 1993; Stephen W. Scheff & Price, 2006; Stephen W. Scheff et al., 2006). However, because synapses are 3D structures, volume electron microscopy (vEM) techniques such as serial block-face electron microscopy (SB-SEM) (Denk & Horstmann, 2004), focused ion beam-scanning electron microscopy (FIB-SEM) (Knott et al., 2008), transmission electron microscope camera array (TEMCA) (Lee et al., 2016) and automated tape-collecting ultramicrotome-electron microscopy (ATUM-EM) (Hayworth et al., 2006; Kasthuri et al., 2015; Shapson-Coe et al., 2021) have become the most widely used tools to generate connectomic datasets. Several studies using FIB-SEM were performed on AD patients' samples and provided information on the number, density, 3D morphology, and organization of synapses (Blazquez-Llorca et al., 2013; Domínguez-Álvaro et al., 2018; Montero-Crespo et al., 2021). The number of synapses showed a decrease, with altered synapse morphology in AD hippocampi (Montero-Crespo et al., 2021). However, due to the limited volume size (usually around 10 µm in x, y, and z) of FIB-SEM data, it was difficult with this method to survey larger volumes that contain full views of neurons. ATUM SEM and TEM have the

capacity to generate large volumes in the cubic millimeter range (MICrONS Consortium et al., 2021; Shapson-Coe et al., 2021) that contain thousands of neurons. A hybrid method named ATUM-FIB was created to provide large-scale context information for local high-resolution FIB volumes and applied on samples from the AD mouse model 5xFAD (Kislinger et al., 2020). Several small-volume (the largest being ~45,000 cubic microns) ATUM-SEM datasets have been generated from Alzheimer's disease rat models (Jiang et al., 2022; Pang et al., 2022), but currently there are no larger vEM volumes (i.e. millions of cubic microns) to provide larger-scale connectomic datasets from either Alzheimer's disease animal models or patients.

In addition to alterations in neuronal connectivity, Alzheimer's disease is associated with the presence of proteinopathies. Two hallmark protein alterations are Aβ and pTau abnormal accumulation in brain parenchyma. The proteolytic cleavage of amyloid precursor protein (APP) produces a variety of Aβ molecules, mainly the 40-amino acid molecule $A\beta_{40}$ and the 42-amino acid molecule $A\beta_{42}$ (G.-F. Chen et al., 2017; Taylor et al., 2002). Aβ molecules exists in various forms (monomer, oligomer, protofibrillar and fibrillar) (G.-F. Chen et al., 2017). Extracellular Aβ can aggregate into dense-core or diffusive plaques that can be identified by EM (Blazquez-Llorca et al., 2013). Aβ can also exist intracellularly, which may be more neurotoxic than extracellular plaques (Gouras et al., 2010; LaFerla et al., 2007). Tau is one of the microtubule-associated proteins (MAPs) that stabilizes microtubules in neurons (Mandelkow & Mandelkow, 1998). Tau is a phosphorylated protein with 85 potential phosphorylation sites on serine, threonine and tyrosine residues (Noble et al., 2013). Under normal conditions, phosphorylation is regulated and affects tau's functions such as its microtubule-binding properties (Mandelkow & Mandelkow, 1998; Noble et al., 2013). Under pathological conditions like AD, tau proteins are hyperphosphorylated (pTau), which causes them to dissociate from microtubules and form aggregates (Mandelkow & Mandelkow, 1998; Noble et al., 2013). pTau can form two forms of neurofibrillary tangles (straight or paired helical filaments) identifiable by TEM (Crowther, 1991). pTau localizes to the cytoplasm, dendrites, and axons, and shows more neurotoxicity in the soluble forms compared to aggregates (Noble et al., 2013). In addition to Aβ and pTau, α-synuclein (Twohig & Nielsen, 2019) and TDP-43 (transactive response DNA-binding protein of 42 kDa) (Wilson et al., 2011) can also form pathological aggregates in AD. Moreover, recent proteomics studies (Johnson et al., 2022, 2020) have

identified multiple protein networks that involve metabolism and activation of glial components that were significantly altered in Alzheimer's disease. On the other hand, recent transcriptomic studies showed alterations in pathways related to neural communication, Aβ clearance (Magistri et al., 2015), and cell-specific stress responses (Mathys et al., 2019). However, currently the causal links between these abnormal proteins or the proteomic and transcriptomic alterations and the manifestation of Alzheimer's disease is circumstantial. One problem is that these molecular alterations have rarely been investigated within the context of the actual neuronal network.

Thus, there is a need for new techniques to localize abnormal proteins or the alterations discovered by proteomic and transcriptomic studies in large-volume electron microscopy studies. Such techniques could pinpoint abnormalities in neuronal networks in Alzheimer's disease and link them to the sites of specific biomolecular (protein or RNA) alterations. However, localization of specific biomolecular features with vEM is challenging. The ultrastructure of synapses in EM micrographs largely relies on intact lipid bilayers. But proteins or mRNAs detection methods like immunofluorescence (Im et al., 2019) and fluorescence in-situ hybridization (Volpi & Bridger, 2008) require the use of detergents (Triton 100-X or Tween 20) that degrade lipid bilayers and degrade ultrastructure of the sample (see below), so vEM carried out subsequently on the same sample suffers from low image quality. To circumvent this challenge, our lab developed a volumetric correlated light and electron microscopy (vCLEM) technology that uses nanobody-assisted, detergent-free immunofluorescence to localize multiple proteins in large ATUM-SEM volumes (Fang et al., 2018). By virtue of their small size (only 1/10 the size of a full-length IgG antibody. See Figure 1 a) and excellent diffusion properties, nanobodies can be used to label intracellular proteins without the need for detergents, so that the ultrastructure of the sample can be preserved (compare Figure 1 b and c). ATUM-SEM can be performed on the same sample to allow superimposition of multi-protein information onto EM micrographs. Three fluorescent nanobody probes for GFAP (astrocyte marker), CD11b (activated microglia marker), and Ly-6C/6G (blood vessel marker) were developed in the study (Fang et al., 2018). This approach should lend itself to further expansion and enable application to the localization of additional Alzheimer's disease related molecules in large-volume connectomic datasets. Proteomic, transcriptomic and connectomic datasets in one and the same sample might thus be bridged.

In this study, we generated two new fluorescent nanobody probes targeting Aβ and pTau respectively. We show that these probes are effective for detergent-free immunofluorescence. We used these two probes, along with other probes that target the microglia marker CD11b, the astrocyte marker GFAP, and the blood vessel marker Ly-6C/6G to label brain tissue samples from the hippocampal CA1 region of an Alzheimer's disease model mouse. We then generated a large-volume vCLEM dataset from one of the labeled samples that retains pristine ultrastructure. With this dataset, we were able to localize extracellular Aβ plaques, intraneuronal Aβ, intracellular pTau at various novel locations, and perform connectomic analysis such as 3D reconstruction of neurons and automatic synapse detection. This new approach will be useful for linking Alzheimer's disease related molecular abnormalities identified by other omics approaches to connectomics abnormalities in the same sample.

Results

Generation of fluorescent nanobody probes for pTau and Aβ

To test the hypothesis that detergent-free immunolabeling by nanobodies could reveal AD-related molecules in a mouse model of AD, we produced a nanobody (also known as A2) specific for tau protein phosphorylated at multiple sites including S422, the most commonly phosphorylated abnormal site and a nanobody (also known as R3VQ) specific for Aβ40/42, both of which were generated in a previous study (Lafaye et al., 2019, 2020; T. Li et al., 2016) for in vivo imaging in AD mouse models. We used a eukaryotic expression system (Expi 293 cells) to express these nanobodies. We added signal peptides to their N'-terminus so that they would be secreted by Expi 293 cells to the culture media for easier purification. We also added sortase tags to their C'-terminus for fluorescent dye conjugation. We purified nanobodies from the culture media by affinity chromatography. Our yields of nanobodies were around 5 mg/ml culture media. We used the sortase reaction (see Material and methods) to add several different fluorescent dyes (5-TAMRA, Alexa Fluor 594, or Alexa Fluor 647) (see Table 1) to the purified nanobodies to obtain the corresponding fluorescent probes.

We tested two red fluorescent (5-TAMRA-conjugated) nanobodies A2 and R3VQ with our detergent-free immunofluorescence protocol (see Material and methods) that preserves fine ultrastructure (Figure 1 c) on tissue sections from the hippocampus CA1 region of 3xTg mice. This AD mouse model

presents with neurofibrillary tangles formed by pTau, Aβ extracellular plaques and intraneuronal Aβ deposits (Oddo et al., 2003).The A2 probe labeled neurofibrillary tangle (NFT)-like structures in the cell bodies and dendrites of certain neurons (Figure 1 d-1, d-2) and the dystrophic neurites nearby plaque material (Figure 1 e-1, e-2). The R3VQ probe labeled extracellular plaque material (Figure 1 f-1, f-2) and the cell bodies of certain neurons (Figure 1 g-1, g-2). In both samples, we found that the nuclear dye Hoechst 33342 labeled extracellular plaque materials as reported before (asterisks in Figure 1 e-2, f-2) (Uchida & Takahashi, 2008). Double immunofluorescence performed on sections from the same region using A2 and the commonly used anti-pTau mAb AT8, or using R3VQ and the commonly used anti-Aβ mAb 4G8 showed colocalization of signals (Sup. Figure a-1 to a-3, b-1 to b-3). No labeling of A2 or R3VQ was observed on sections from the same region of age-matched control animals (Sup. Figure 1 c to f). Therefore, we believe that the fluorescent conjugated A2 and R3VQ can be used as immunolabeling probes for Aβ and pTau for detergent-free immunofluorescence.

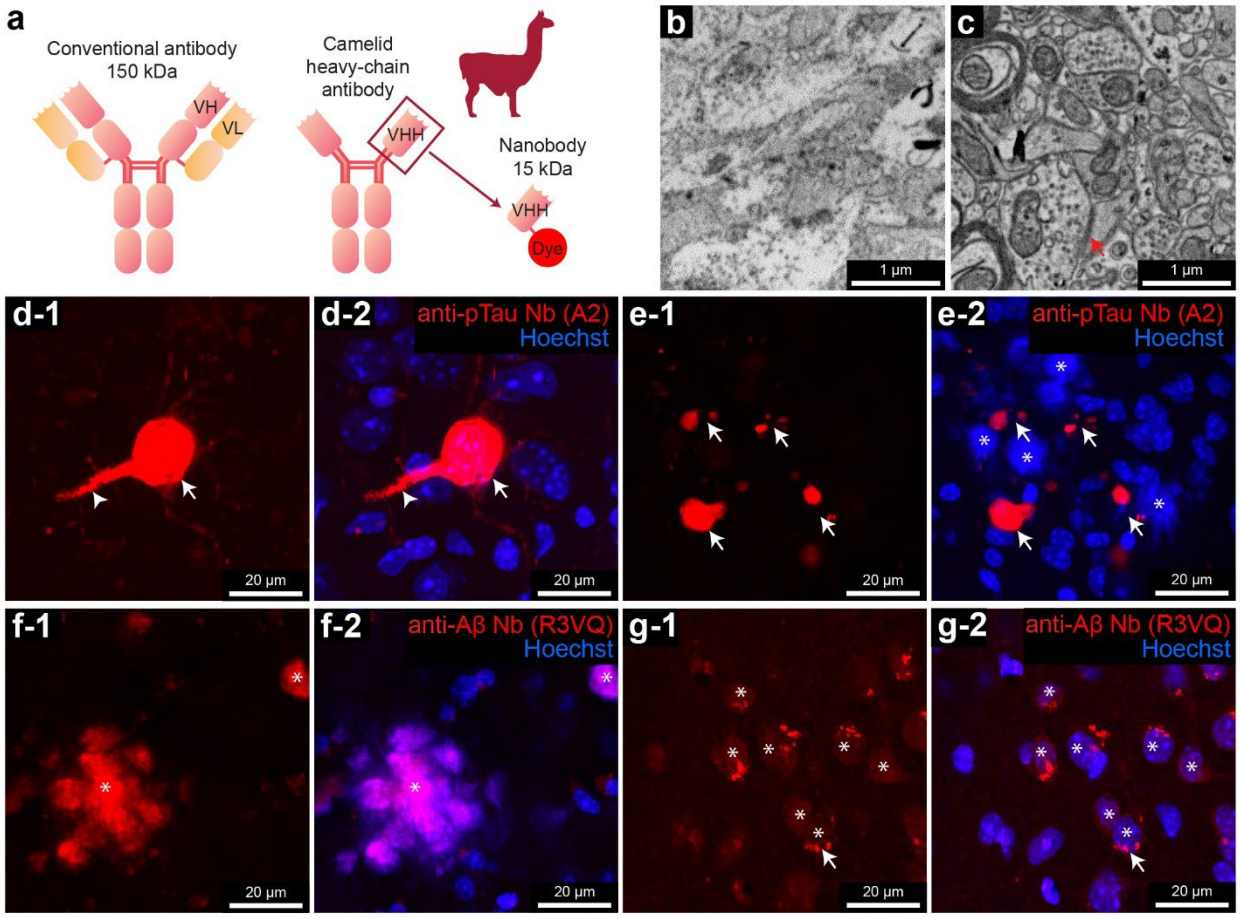

Figure 1. Characterization of fluorescent nanobody probes for pTau and Aβ.

a, Schematic representations of a full-length IgG antibody, a camelid antibody, and a nanobody probe with a conjugated fluorescent dye. **b**-**c**, Comparison of ultrastructure between a sample (**b**) treated by Triton X-100 and a sample (**c**) labeled by nanobody probes, untreated with Triton X-100. Red arrow in **c** indicates a synapse. **d-1** to **e-2**, Confocal images from the hippocampus of a 3xTg mouse labeled with a pTau-specific nanobody probe (A2) conjugated with the red dye 5-TAMRA. Arrows in **d-1** and **d-2** show the labeled neuronal cell body. Arrowheads in **d-1** and **d-2** show the labeled apical dendrite. Arrows in **e-1** and **e-2** show the labeled neurites. Asterisks in **e-2** show the plaque material labeled by Hoechst. **f-1** to **g-2**, Confocal images from the hippocampus of a 3xTg mouse labeled with an Aβ-specific nanobody probe (R3VQ) conjugated with the red dye 5-TAMRA. Asterisks in **f-1** and **f-2** show the labeled plaque material. Asterisks in **g-1** and **g-2** show the labeled neuronal cell bodies. Arrows in **g-1** and **g-2** show the autofluorescent lipofuscin.

Table 1. Fluorescent nanobody immuno-probes generated in this work.

Target	Clone No.	Source	Fluorescent dyes conjugated
pTau	A2	(T. Li et al., 2016)	5-TAMRA, Alexa Fluor 594, Alexa Fluor 647
Aβ 40/42	R3VQ	(T. Li et al., 2016)	5-TAMRA, Alexa Fluor 647

Localization of multiple AD-related molecules with fluorescent nanobody probes

Three fluorescent nanobody probes were developed (Fang et al., 2018) targeting three AD related molecules: CD11b, a membrane protein expressed at high level by activated microglia in AD; GFAP, glial fibrillary acidic protein, an intracellular protein expressed at high level by activated astrocytes in AD; Ly-6C/6G, a lymphocyte antigen expressed by endothelial cells of blood vessels, which can be used to detect vascular abnormalities in AD. We proceeded to test if we could combine the new probes for pTau and Aβ with these three nanobody probes to achieve multi-color labeling with our detergent-free immunofluorescence protocol.

We used three fluorescent nanobody probes (anti-CD11b-Alexa Fluor 488, anti-pTau-5-TAMRA or A2, and anti-Aβ40/42-Alexa Fluor 647 or R3VQ) to simultaneously label two 120-μm thick coronal brain sections at Bregma -3.78 mm and -3.28 mm in the absence of detergent (Figure 2 a, b; see Sup. Figure 2 for the anatomical details of the labeled sections) of a one-year-old female 3xTg mouse. We acquired a four-color fluorescence image stack of 57 μm (Figure 2 a) from the first section and a 21-μm stack from the second section (Figure 2 b; see Sup. Figure 2 for the anatomical details of the imaged regions of interest) in the stratum pyramidale of the hippocampal CA1 region.

Because the red fluorescence signal from the anti-pTau probe was far stronger than the green signal from the anti-CD11b probe, we saw crosstalk in the green channel. This meant that in the overlay, the pTau label appears yellow whereas the microglia appear green, but the two labels were nonetheless unambiguous. Another issue was that aged mice have lipofuscin (Figure 2 c, d) particles in cell bodies of neurons and glia. This non-specific fluorescence localized to inclusion bodies that were easily differentiated from the membrane labeling of microglia.

In both image stacks, NFT-like structures in the cell bodies and dendrites of certain pyramidal neurons and some dystrophic neurites were labeled by the anti-pTau probe (yellow signals in Figure 2 c, d); intraneuronal Aβ of certain pyramidal neurons were labeled by the anti-Aβ probe (magenta signals in Figure 2 c, d); activated microglia were labeled by the anti-CD11b probe (green signals in Figure 2 c, d). We noted that these labeled structures/cells were more abundant, and the labeled apical dendrites appeared to be more tortuous in the image stack acquired from the Bregma -3.78 mm section (Figure 2 c, d). Only in the first image stack (Figure 2 a, c) acquired from this section did we find five extracellular Aβ

plaques labeled by the anti-Aβ 40/42 probe (magenta signals in Figure 2 a, c). These findings are consistent with the fact that the pathologies of neurofibrillary tangles and Aβ plaques progress from caudal to rostral in the hippocampus in the 3xTg mice (Belfiore et al., 2019).

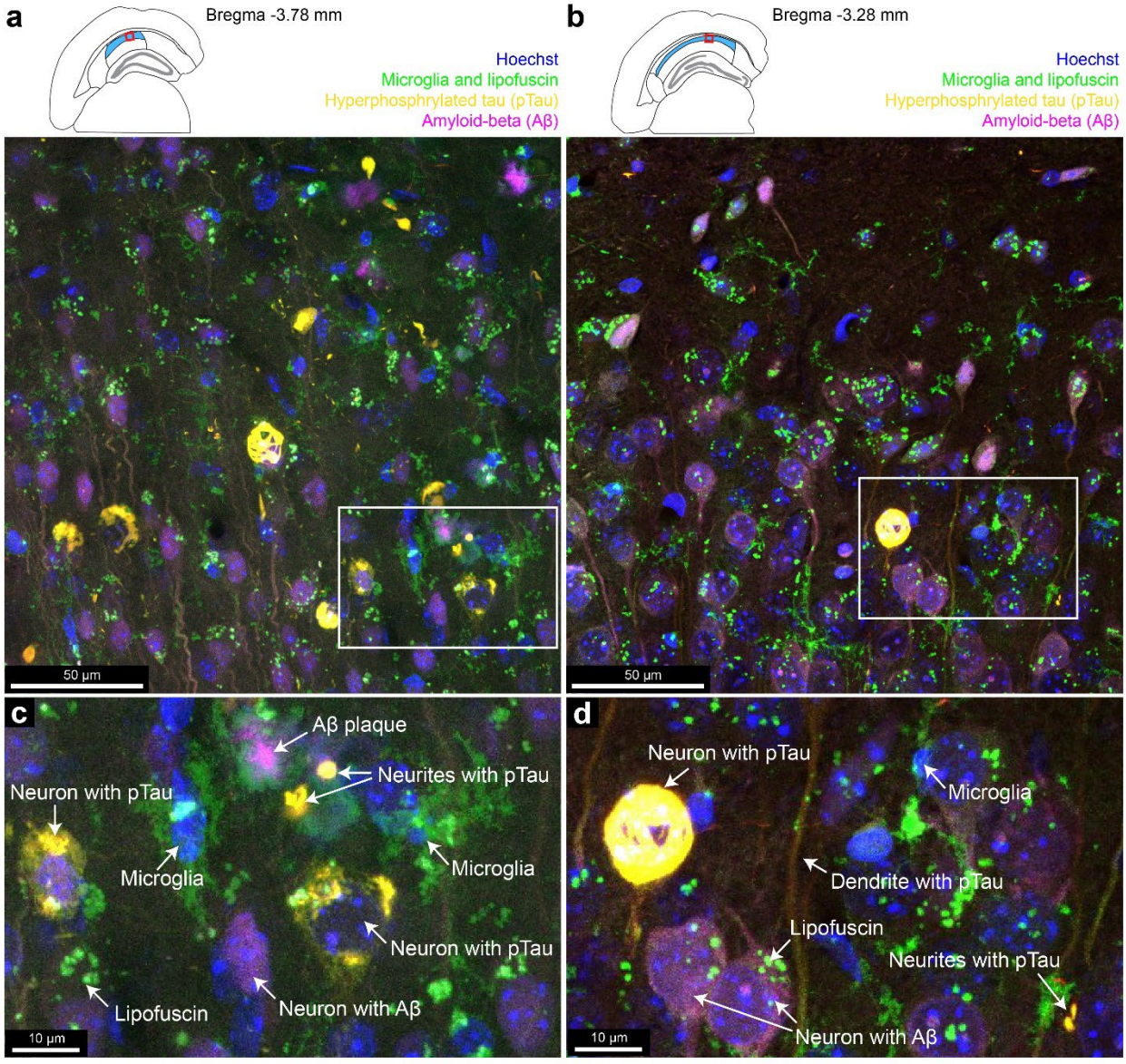

Figure 2. Four-color detergent-free immunofluorescence enabled by nanobody probes.

Maximum intensity projection of the multi-color fluorescence image stacks acquired from the hippocampus at the Bregma -3.78 mm (**a**) or the Bregma -3.28 mm (**b**) of a 3xTg mouse labeled with a CD11b-specific nanobody probe conjugated with Alexa Fluor 488, a pTau-specific nanobody probe conjugated with 5-TAMRA, and an Aβ-specific nanobody probe conjugated with Alexa Fluor 647. Red boxes in the coronal section illustrations show where the image stacks were acquired. The stratum pyramidale of the hippocampal CA1 region is labeled in blue in the illustrations. **c-d**, enlarged boxed

insets from **a**-**b**.

We also acquired a five-color fluorescence image stack of 23 µm (Figure 3) in the same region from a 120-µm thick coronal section at Bregma -3.78 mm of another one-year-old female 3xTg mouse. This section was simultaneously labeled by four fluorescent nanobody probes (anti-CD11b-Alexa Fluor 488, anti-GFAP-5-TAMRA, anti-pTau-Alexa Fluor 594 or A2, and anti-Ly-6C/6G-Alexa Fluor 647) without the usage of detergent. We found numerous activated astrocytes labeled by the anti-GFAP nanobody probe nearby extracellular plaque material and neurons/neurites that have pTau (yellow signals in Figure 3 a, b). Interestingly, we found that in addition to labeling blood vessels, the anti-Ly-6C/6G probe also labeled some but not all plaque material (arrows in Figure 3 d) surrounded by activated microglia labeled by the anti-CD11b probe (green signals in Figure 3 d).

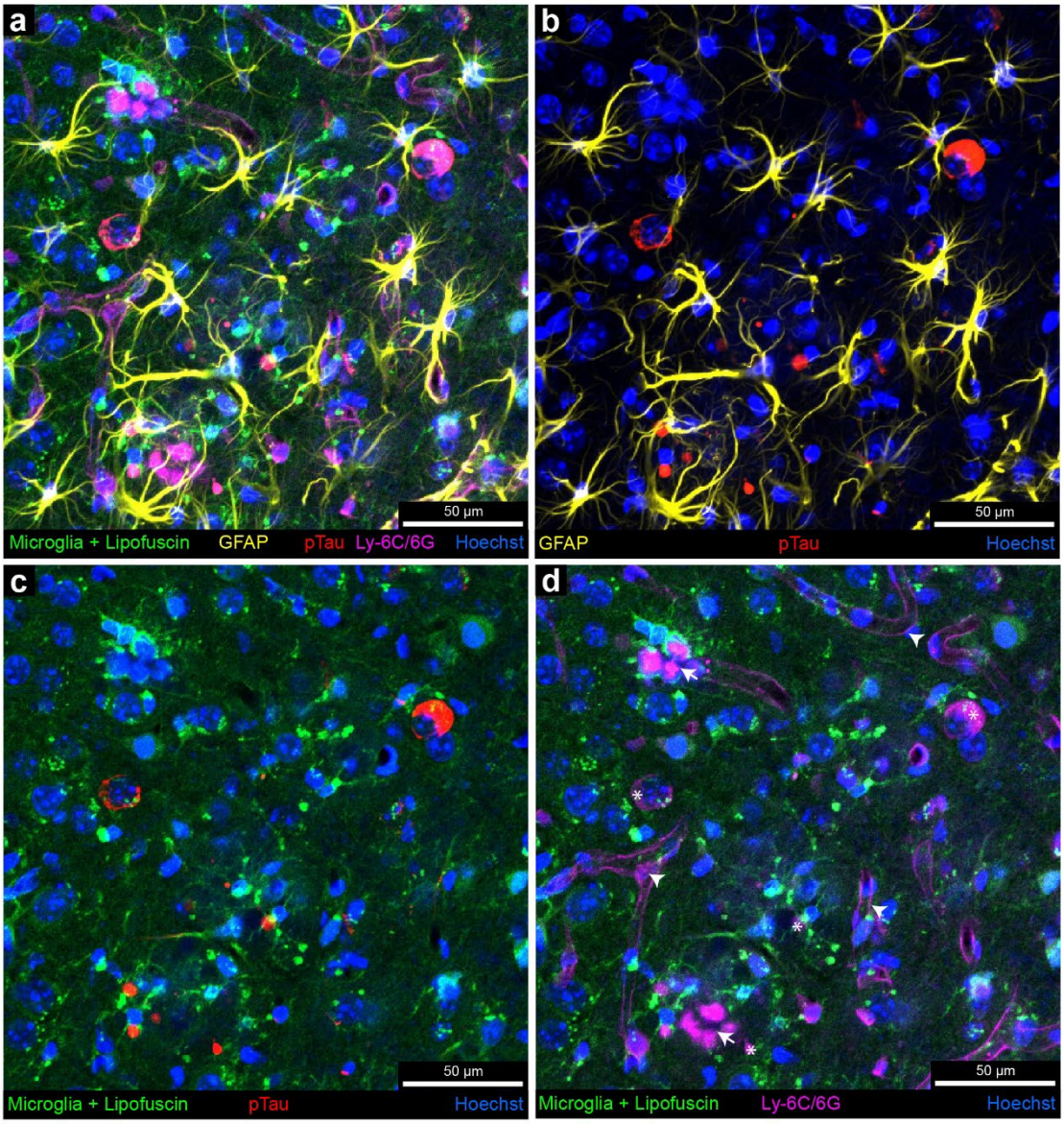

Figure 3. Five-color detergent-free immunofluorescence enabled by nanobody probes.

a, Maximum intensity projection of the multi-color fluorescence image stacks acquired from the hippocampus of a 3xTg mouse labeled with a CD11b-specific nanobody probe conjugated with Alexa Fluor 488, a GFAP-specific nanobody probe conjugated with 5-TAMRA, a pTau-specific nanobody probe conjugated with Alexa Fluor 594, and a Ly-6C/6G-specific nanobody probe conjugated with Alexa Fluor 647. The signal of each fluorescent dye was pseudo-colored for better visualization. **b**-**d**, Three-channel maximum intensity projection images of the multi-color fluorescence image stack. Arrows in **d** show the labeled plaque material by the anti-Ly-6C/6G nanobody probe. Arrowheads in **d** show the labeled blood vessels by the anti-Ly-6C/6G nanobody probe. Asterisks in **d** show the crosstalk signals from the anti-pTau labeling.

Multi-color, large-scale vCLEM reveals ultrastructural abnormalities labeled by nanobody probes

After confocal imaging, the section in Figure 2 a was stained with heavy metals, embedded in

resin, and imaged by X-ray CT (microCT). The image volume acquired by microCT showed regions with Aβ plaques and neuronal degeneration (Sup. Figure 3) as reported before (Barbone et al., 2022). After X-ray scanning, the sample was sectioned into serial 30-nm ultrathin sections by ATUM and imaged by scanning electron microscopy (see Materials and methods). We used a multi-beam scanning electron microscope to acquire a high-resolution image volume of 245 µm x 238 µm x 23 µm at a resolution of 4 nm x 4 nm x 30 nm (Figure 4 a). As far as we know, it is the largest vEM volume ever acquired from an AD mouse model. The ultrastructure was well preserved throughout the image volume (Figure 4 b), which enabled the identification of synapses (Figure 4 b, red arrow).

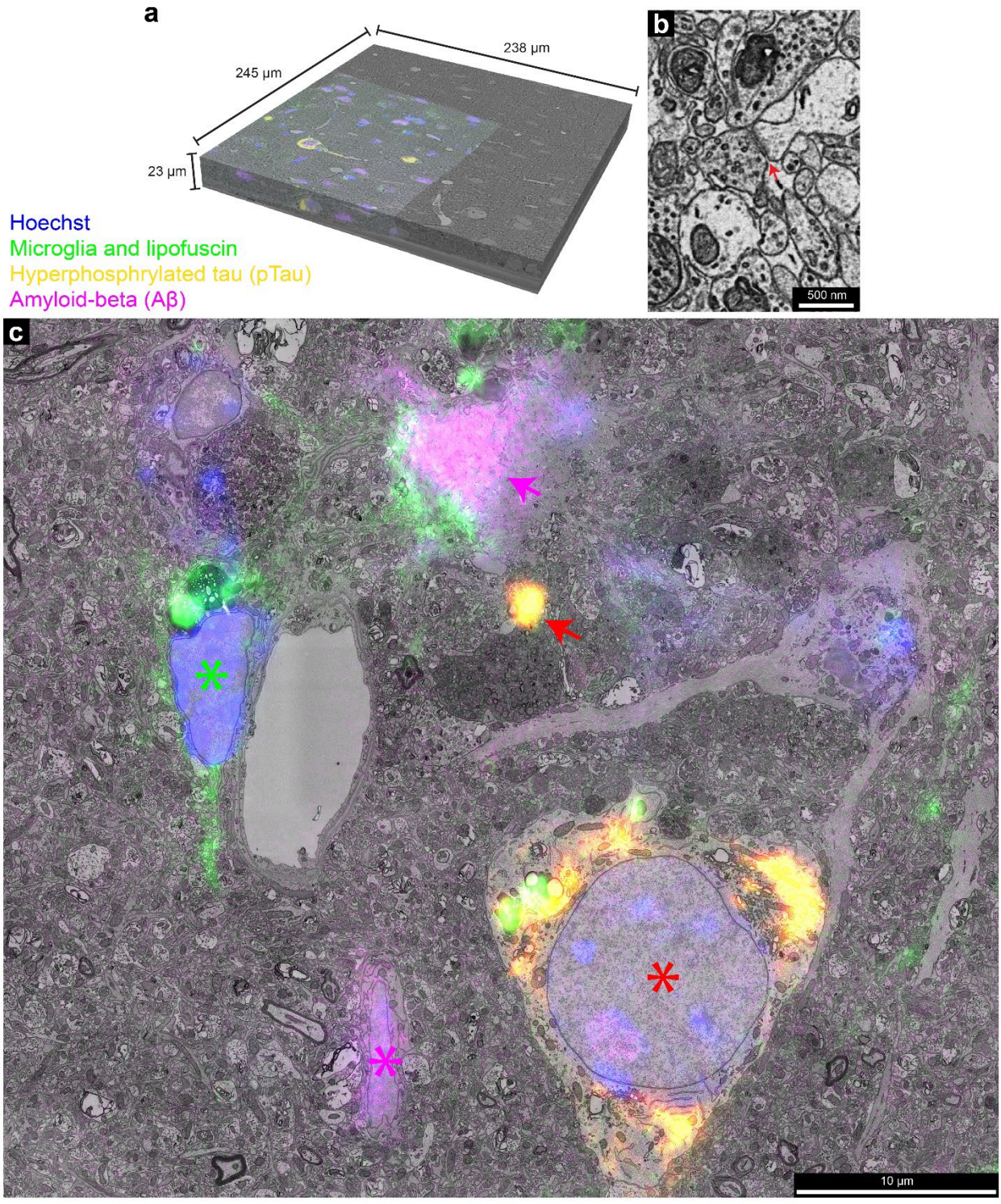

Figure 4. Four-color VCLEM enabled identification of ultrastructural abnormalities related to the nanobody labeling.

a, The high-resolution vEM volume acquired from the hippocampus CA1 region with four-color immunofluorescence from nanobody probes. The four-color fluorescence data was co-registered with the

high-resolution vEM data. **b**, the preserved ultrastructure from this vEM volume. Red arrow shows a synapse. **c**, Demonstration of the overlay between fluorescence signals and EM ultrastructure. The red asterisk indicates the cell body of a pyramidal neuron labeled by the anti-pTau nanobody. The red arrow indicates the dystrophic neurite labeled by the anti-pTau nanobody. The magenta arrow indicates the plaque material labeled by the anti-Aβ nanobody. The magenta asterisk indicates the cell body of a pyramidal neuron labeled by the anti-Aβ nanobody. The green asterisk indicates the microglia labeled by the anti-CD11b nanobody.

A high-precision co-registration between the fluorescence image stack and the high-resolution EM image volume was based on finding corresponding sites (blood vessels, cell nuclei) in the two volumes. We used the FIJI/ImageJ plugin BigWarp (Bogovic et al., 2016) to perform a 3D transformation of the fluorescence stack via thin plate spline interpolation to register the volumes. The transformed fluorescence volume overlaid onto 1/3 of the high-resolution EM volume is shown in Figure 4 a. We localized the fluorescence signals from each molecular marker to the EM ultrastructure (Figure 4 c). Figure 4 c shows a region of interest on one slice in which pTau (yellow) overlaps with the cell body of a pyramidal neuron and a dystrophic neurite, Aβ (magenta) overlaps with an Aβ plaque and the cell body of another pyramidal neuron, and CD11b (green) overlaps with a microglial cell. This region is the same as what is shown in Figure 2 c. We ingested this vCLEM dataset into Neuroglancer. Users can visualize each fluorescence channel and the EM channel separately or simultaneously, and navigate through slices at different resolution levels. Any researcher can access this dataset in Neuroglancer by this link.

We proceeded to analyze the sites labeled with each of the three molecular markers (pTau, Aβ, CD11b) in this vCLEM dataset.

pTau: We found NFT-like structures from the labeling of the anti-pTau nanobody localized within cell bodies of seven pyramidal neurons and one glial cell (red fluorescence, see Figure 5 a-1 to d-2 for four examples) among the ~100 neuronal and glial cells in the volume where the fluorescence signals were co-registered. Two of the pyramidal cells also showed intraneuronal Aβ (magenta fluorescence, see Figure 5 d-2 for one example). Only one of the seven pTau positive pyramidal cells (which incidentally did not show intraneuronal Aβ), showed pathological straight filament-like structures (Figure 5 a-1, a-2; Sup. Figure 4 a), which is one of the ultrastructural manifestations of neurofibrillary tangles (Crowther, 1991). The other pTau positive pyramidal cells showed short filament-like structures in their cell bodies (Figure 5 b-2, c-2). We suspect that these are not pathological because in other pyramidal neurons free of pTau

labeling, similar structures were seen (Sup. Figure 4 c-1, c-2). Two pyramidal neurons that were both pTau and Aβ positive (see Figure 5 d-1, d-2 for one example) had the same morphological features as neurons that only had intraneuronal Aβ (see below). We also found NFT-like structures localized in dendrites that were either straight or tortuous (Figure 5 e-1 to f-2). Again, we did not find specific ultrastructural manifestations of the neurofibrillary tangle structures in these dendrites despite them being pTau positive (Sup. Figure 4 d-1, d-2). We examined a total of three axons (two originating from pTau positive pyramidal cells in the volume). One of these possessed two pTau positive bleb-like structures each filled with straight filaments (see Figure 5 g-1, g-2; see Sup. Figure 4 for one of them); another axon had an enlarged pTau positive swelling filled with lipofuscin granules (Figure 5 h-1, h-2); and one terminated in a large pTau positive bleb-like structure filled with degenerating organelles emerging from a myelinated axon (Figure 5 i-1, i-2) as has been seen previously (Gowrishankar et al., 2015). The labeled glial cell had glial inclusions known as “coiled bodies” (Ferrer et al., 2014; T. Li et al., 2016) which were specifically labeled by the anti-pTau probe (Figure 5 j-1, j-2). Based on the fact that we did not find the typical ultrastructural representations at all sites that had pTau, we believe that some types of NFT-like structures or pTau aggregates do not have observable ultrastructural representations. This shows that it is necessary to rely on labeling techniques such as ours to detect neurons that harbor these structures in EM micrographs.

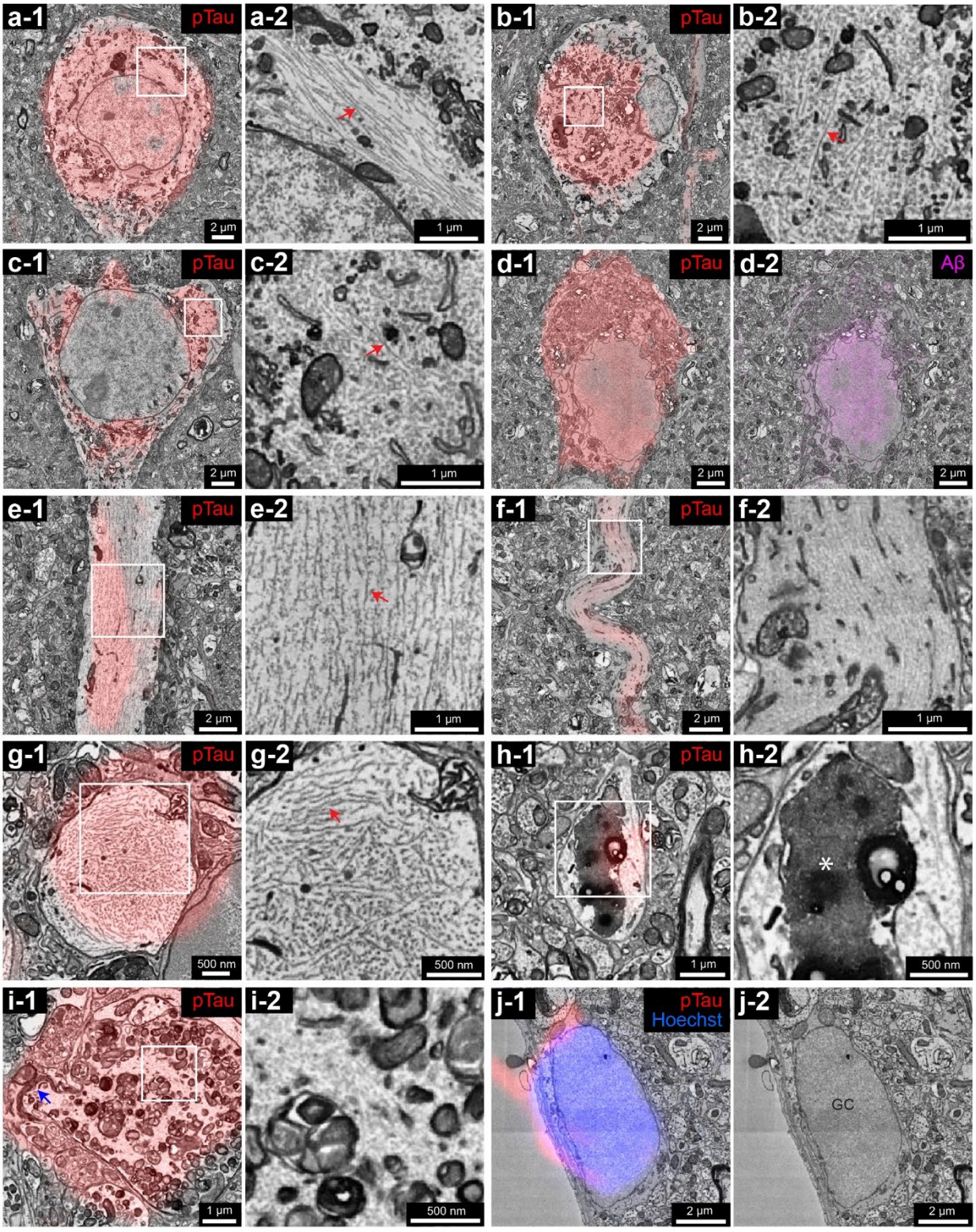

Figure 5. Ultrastructural abnormalities related to the anti-pTau nanobody labeling.

a-1, red fluorescence from the anti-pTau nanobody overlaps with the cell body of a pyramidal neuron. **a-2**,

enlarged inset from **a-1**. Red arrow indicates the straight filament-like structure. **b-1** and **c-1**, red fluorescence from the anti-pTau nanobody overlaps with the cell bodies of two pyramidal neurons. **b-2** and **c-2**, enlarged insets from **b-1** and **c-1**. Red arrows indicate the short filament-like structures that were also seen in neurons that were not labeled by the anti-pTau nanobody (see Sup. Figure 4 c-1, c-2). **d-1** and **d-2**, the pyramidal neuron that was labeled by both the anti-pTau nanobody (red fluorescence in **d-1**) and the anti-Aβ nanobody (magenta fluorescence in **d-2**). **e-1** and **f-1**, red fluorescence from the anti-pTau nanobody overlaps with a straight apical dendrite and a tortuous apical dendrite of two pyramidal neurons. **e-2** and **f-2**, enlarged insets from **e-1** and **f-1**. The red arrow in **e-2** indicates the short filament-like structure that was also seen in apical dendrite that was not labeled by the anti-pTau nanobody (see Sup. Figure 4 d-1, d-2). **g-1**, red fluorescence from the anti-pTau nanobody overlaps with a bleb-structure connected to an axon. **g-2**, enlarged inset from **g-1**. Red arrow indicates the straight filament-like structure. **h-1**, red fluorescence from the anti-pTau nanobody overlaps with an enlarged swelling of an axon filled with lipofuscin granules. **h-2**, enlarged inset from **h-1**. Asterisk shows the lipofuscin granules. **i-1**, red fluorescence from the anti-pTau nanobody overlaps with a bleb-like structure that emerged from a myelinated axon. This bleb was filled with degenerating organelles. Blue arrow indicates the end of the myelination. **i-2**, enlarged inset from showing the degenerating organelles. **j-1** and **j-2**, red fluorescence from the anti-pTau nanobody overlaps with a glial cell that had coiled bodies (red fluorescence in **j-1**).

Aβ: We found extracellular Aβ plaque structures from the labeling of the anti-Aβ nanobody (magenta fluorescence in Figure 6) localized within five separate spots of plaque material (see Figure 6 a-1 to b-2 for two examples) which showed the typical ultrastructure of dense-cored plaques (Blazquez-Llorca et al., 2013). These plaques had dense cores of Aβ deposits in the center, Aβ fibrils, glial processes and dystrophic neurites surrounding them. Intraneuronal Aβ localized within neurons that had very tortuous apical dendrites, shrunken cell bodies, dark osmiophilic cytoplasm and degenerating organelles (Figure 6 c-1 to d-2). These neurons with intraneuronal Aβ appeared to be more abnormal than neurons that only had pTau.

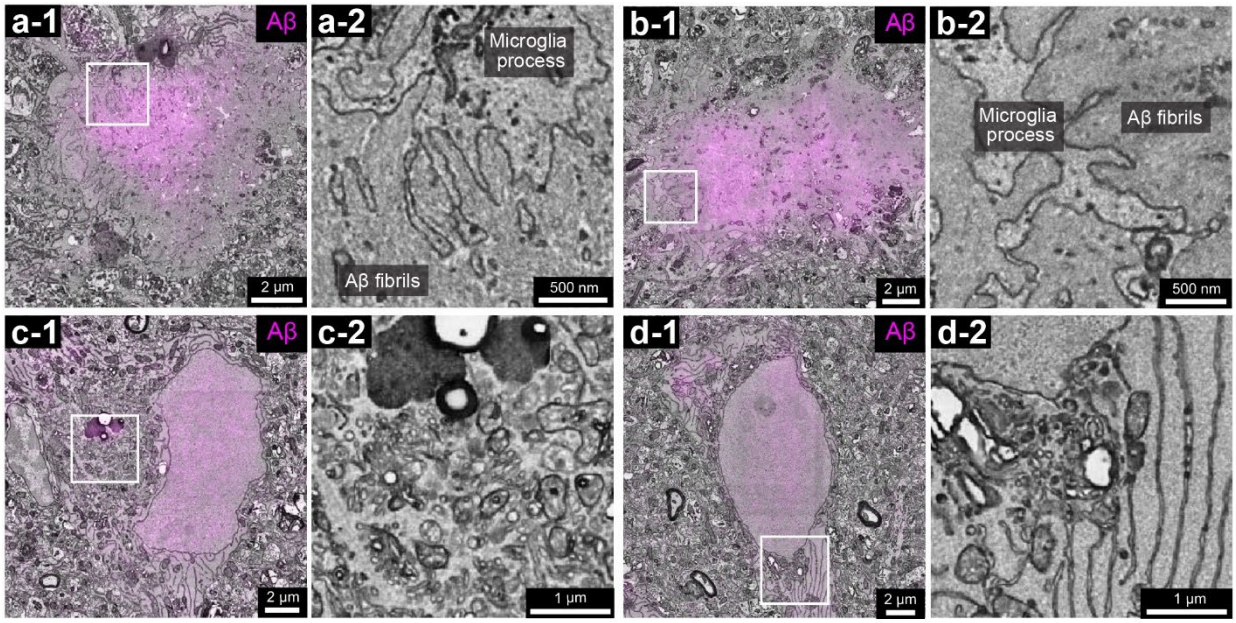

Figure 6. Ultrastructural abnormalities related to the anti-Aβ nanobody.

a-1, magenta fluorescence from the anti-Aβ nanobody overlaps with plaque material. **a-2**, enlarged inset from **a-1**. **b-1**, magenta fluorescence from the anti-Aβ nanobody overlaps with another plaque material. **b-2**, enlarged inset from **b-1**. **c-1**, magenta fluorescence from the anti-Aβ nanobody overlaps with the cell body of a pyramidal neuron. **c-2**, enlarged inset from **c-1** showing the degenerating organelles in this neuron. **d-1**, magenta fluorescence from the anti-Aβ nanobody overlaps with the cell body of another pyramidal neuron. **d-2**, enlarged inset from **d-1** showing the dilated endoplasmic reticula in this neuron.

CD11b: This molecule is a component of the phagocytic receptor CR3, which localizes to the cell membrane of activated microglia (Bisht et al., 2016). These microglia were named “dark microglia” in a previous electron microscopy study owing to their condensed, electron-dense cytoplasm and nucleoplasm (Bisht et al., 2016). In our vCLEM dataset, we identified 10 microglia (see Figure 7 for five examples) based on the labeling with the anti-CD11b nanobody (green fluorescence in Figure 7). Among them, five were associated with Aβ plaques (Figure 7 a-1, c-3, c-4), extending ramified processes to encircle and perhaps phagocytose plaque material (Figure 7 b); four however were associated with dystrophic neurites where there was no Aβ plaque (Figure 7 c-1); one was adjacent to a neuron that had intraneuronal Aβ (Figure 7 c-2). These microglia appeared stressed: they had a large amount of lipofuscin granules, osmiophilic cytoplasm, altered mitochondria, condensed nucleoplasm, and dilated endoplasmic reticulum (Figure 7 a-2, a-3), as previously described (Bisht et al., 2016).

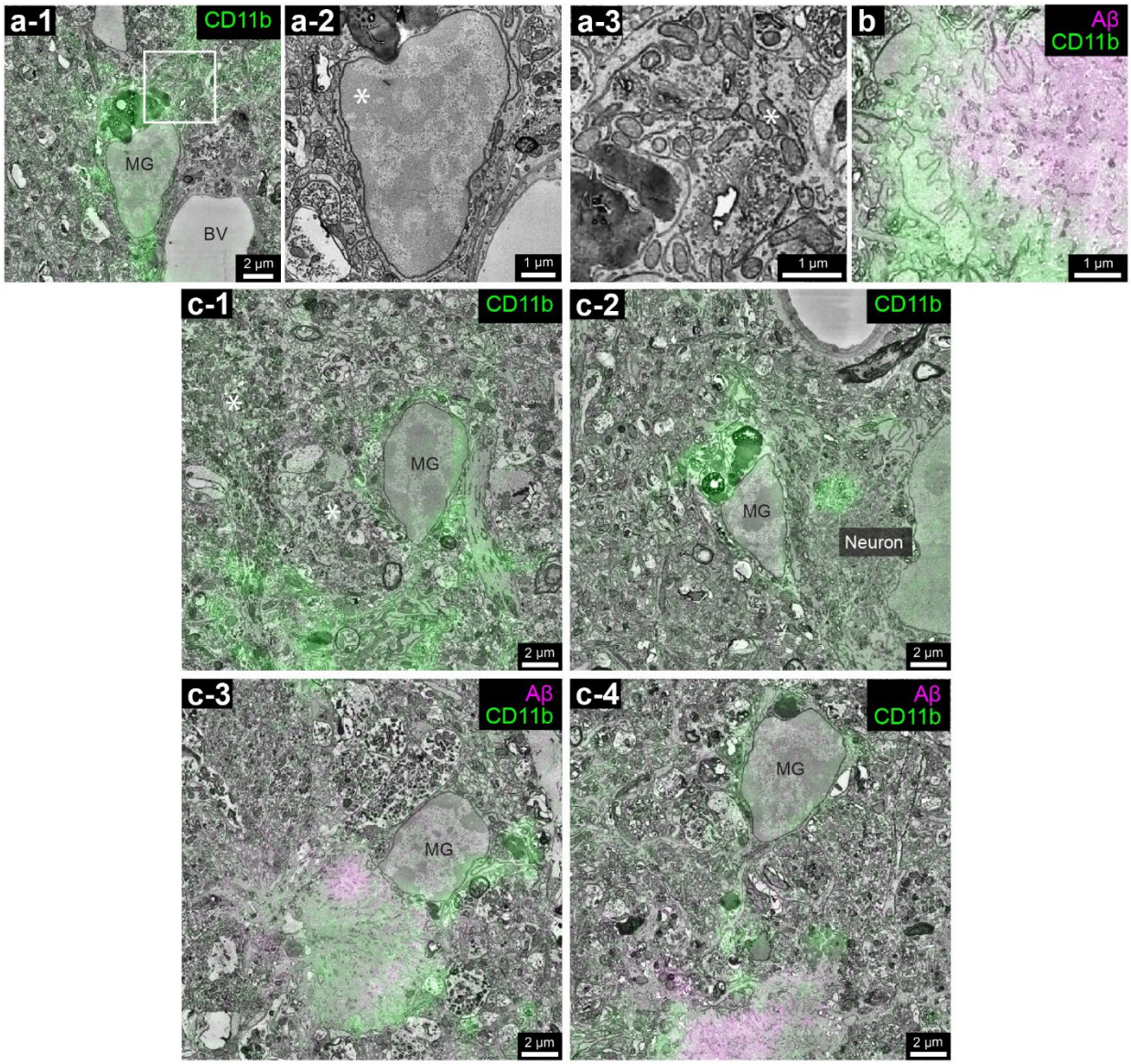

Figure 7. Ultrastructural abnormalities related to the anti-CD11b nanobody.

a-1, green fluorescence from the anti-CD11b nanobody overlaps with a microglial cell. **a-2**, the nucleus of the microglial cell in **a-1**. Asterisk indicates the condensed nucleoplasm. **a-3**, enlarged inset from **a-1**. Asterisk indicates the altered mitochondria. **b**, green fluorescence from the anti-CD11b nanobody overlaps with the glial processes encircling plaque material, which shows overlapped magenta fluorescence from the anti-Aβ nanobody. **c-1**, green fluorescence from the anti-CD11b nanobody overlaps with a microglial cell nearby dystrophic neurites (asterisks). **c-2**, green fluorescence from the anti-CD11b nanobody overlaps with a microglial cell next to a pyramidal neuron (the same neuron in Figure 6 c-1). **c-3** and **c-4**, green fluorescence from the anti-CD11b nanobody overlaps with two microglial cells nearby plaque material, which shows overlapped magenta fluorescence from the anti-Aβ nanobody.

3D reconstructions of neurons with intraneuronal Aβ or pTau show morphological abnormalities

In order to carry out connectomic study on large vEM datasets, it was necessary to segment the image data automatically to make analysis more efficient. We used a flood-filling network (FFN) (Michał Januszewski et al., 2018) pretrained on the H01 dataset (Shapson-Coe et al., 2021) without additional new ground truth from this AD data. The direct application of the pre-trained FFN to this dataset was sufficiently good to segment neuronal cell bodies and dendrites but failed to segment axonal and glial processes. Therefore we used Segmentation Enhanced CycleGAN (Michal Januszewski & Jain, 2019) to modify the visual appearance of this dataset to the H01 dataset and then applied the pre-trained FFN, which improved the segmentation of axonal and glial processes.

Unlike previously described FIB-SEM/ATUM-SEM datasets acquired from AD tissue samples (Blazquez-Llorca et al., 2013; Domínguez-Álvaro et al., 2018; Jiang et al., 2022; Montero-Crespo et al., 2021; Pang et al., 2022) that only allowed 3D reconstruction of synapses or small segments of dendrites and axons, this dataset has much larger dimensions, making it possible to 3D reconstruct neurons more completely. Using the automatic segmentation followed by manual proofreading, a pyramidal neuron with intraneuronal Aβ (Figure 6 c-1) and two pyramidal neurons with intraneuronal pTau (Figure 5 b-1, c-1) were reconstructed.

The cell body of neuron 1 with intraneuronal Aβ labeling appeared abnormal as if it were in the process of degenerating (Figure 6 c-1, c-2). A microglial cell was immediately adjacent raising the possibility that the neuron would soon be phagocytosed (Figure 7 c-2). Surprisingly, this neuron still retained multiple spiny dendrites (Figure 8 a, inset 1) and its axon projected normally for ~100 µm without myelin and then showed normal myelination (Figure 8 a). Neuron 2 showed intraneuronal pTau labeling in its soma (Figure 5 b-1, b-2). Nonetheless it also had multiple normal looking spiny dendrites (Figure 8 a, inset 2). This neuron's axon ran normally ~80 µm before becoming myelinated (Figure 8 a). As was the case for the other two neurons, there were several spine-like structures innervated by vesicle-filled axonal profiles (Figure 8b) along this neuron's axon initial segment (AIS). This AIS also had an abnormally enlarged swelling that was positive for anti-pTau nanobody labeling. This swelling was filled with lipofuscin granules (see Figure 5 h-1, h-2). The third neuron (Neuron 3) with intraneuronal pTau labeling (Figure 5 c-1, c-2) was located such that its soma was adjacent to an Aβ plaque (Figure 8 a). This neuron

also possessed multiple normal looking spiny dendrites (Figure 8 a inset 3) and an axon with normal appearance that ran ~60 µm before becoming myelinated (Figure 8 a). Two spine-like swollen protrusions emerged from its AIS via narrow stalks (Figure 8 a box c, d-1, d-2; Figure 8 c). Each of these was filled with straight filaments, similar to those described above (Figure 8 d-1, d-2; also see Figure 5 g-1, g-2 and Sup. Figure 4 b). We suspect that these objects are abnormally enlarged postsynaptic spine heads because they were innervated by vesicle-filled axonal profiles (Figure 8 e-1, e-2).

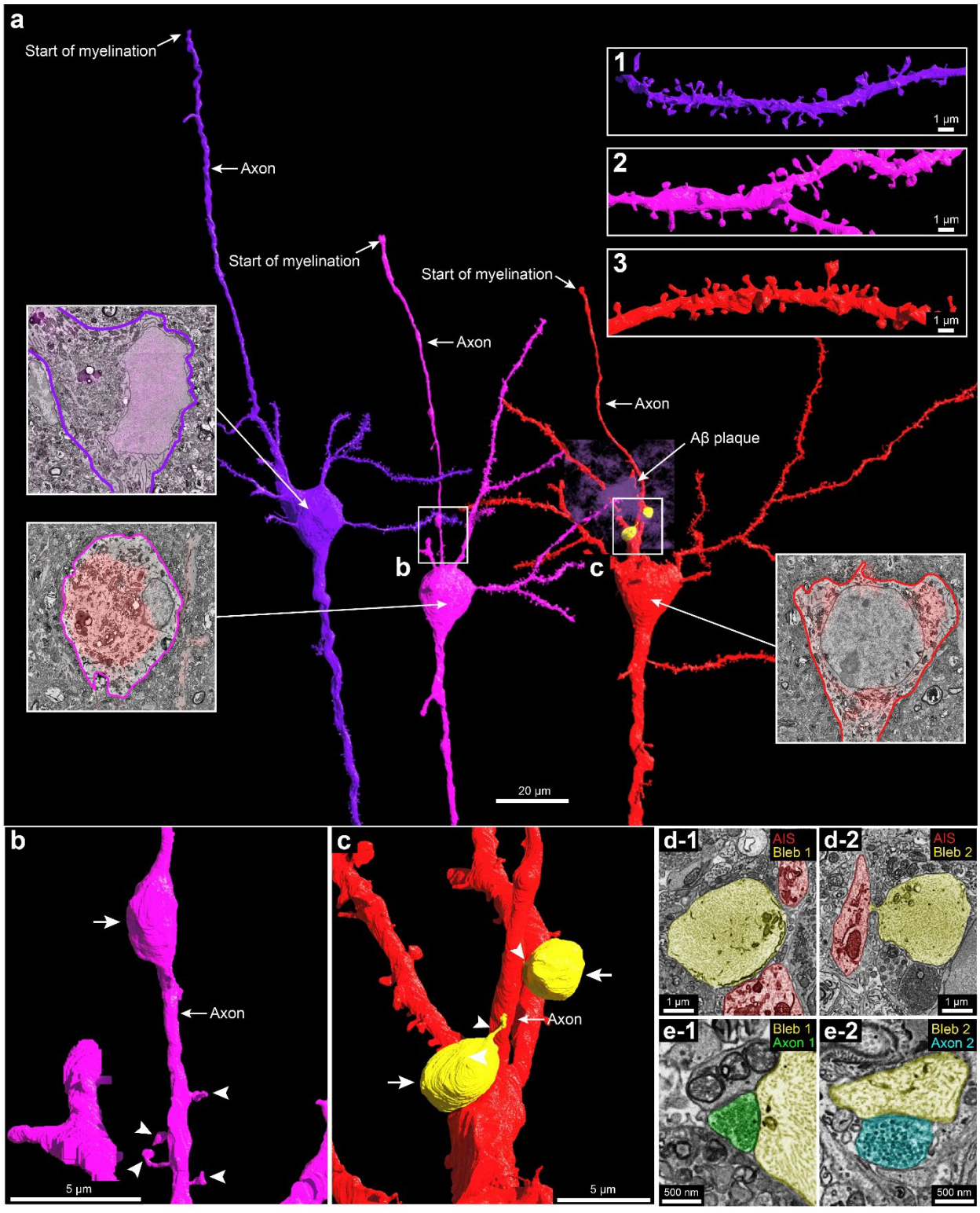

Figure 8. 3D reconstruction of a neuron with intracellular Aβ and a neuron with intracellular NFT-like structure.

a, 3D reconstruction of three pyramidal neurons. The insets pointing to the cell bodies show the labeling

of Aβ or pTau by nanobody probes. Insets 1 to 3 show segments of spiny dendrites of Neuron 1 to 3. **b** shows the AIS of Neuron 2 as labeled in **a**. White arrow, the swelling filled with pTau. White arrow heads, spines on AIS. **c** shows the AIS of Neuron 3 as labeled in **a**. White arrows, two pTau positive blebs connected to the AIS. White arrows, thin stalks connecting the blebs to the AIS. **d-1** and **d-2**, 2D segmentations of the two pTau positive blebs filled with straight filaments. **e-1** and **e-2** show that each of the blebs was adjacent to an axon profile filled with synaptic vesicles.

Machine-learning-based synapse detection reveals alterations in synapse density and size near a Aβ plaque

In addition to pathologies like Aβ plaques and NFT, numerous studies (Blazquez-Llorca et al., 2013; DeKosky & Scheff, 1990; Domínguez-Álvaro et al., 2018; Montero-Crespo et al., 2021; S. W. Scheff et al., 1990; S. W. Scheff & Price, 1993; Stephen W. Scheff & Price, 2006; Stephen W. Scheff et al., 2006) have suggested synaptic alterations in AD. Indeed cognitive decline in Alzheimer's disease appears to correlate with a decline in synapse density (DeKosky & Scheff, 1990; Harbaugh et al., 1989). This vCLEM dataset has the necessary resolution to locate and analyze synapses ultrastructurally (Figure 1 c and Figure 4 b). Although manual annotation to analyze synapses is straightforward, it is not ideal for analysis of their density as a function of proximity to a plaque, given their large number. Machine-learning-based automated synapse detection (Buhmann et al., 2021; Çiçek et al., 2016; Lin et al., 2021; Parag et al., 2019; Santurkar et al., 2017; Staffler et al., 2017; Su et al., 2023) has been performed on large-scale connectomics datasets (Scheffer et al., 2020; Shapson-Coe et al., 2021; Turner et al., 2022) and proved to be time-efficient, unbiased and accurate.

Using a U-Net classifier (Çiçek et al., 2016) that was trained on a human cortex vEM dataset, we identified many of the synapses in the vCLEM dataset (Figure 9 a). However, there were undetected synapses (i.e., false negatives, Figure 9 a, arrows) and there were false positive detections inside neuronal processes (Figure 9 a, arrowheads). To help solve these problems we carried out automatic 2D cell membrane detection with mEMbrain (Pavarino et al., 2023) (Figure 9 b) and then dilated the detected cell membranes as a filter to only keep the synaptic detections that were associated with the neuronal membranes. This strategy proved effective in eliminating most false positive detections (compare Figure 9 a and c). We applied the filtering method in a box with the dimensions of 90 µm x 90 µm x 6 µm near an Aβ plaque. The 3D rendering of the detected synapses (Figure 9 d and e) permits synapse detection on a large scale of hundreds of micrometers but still leaves a number of synapses undetected.

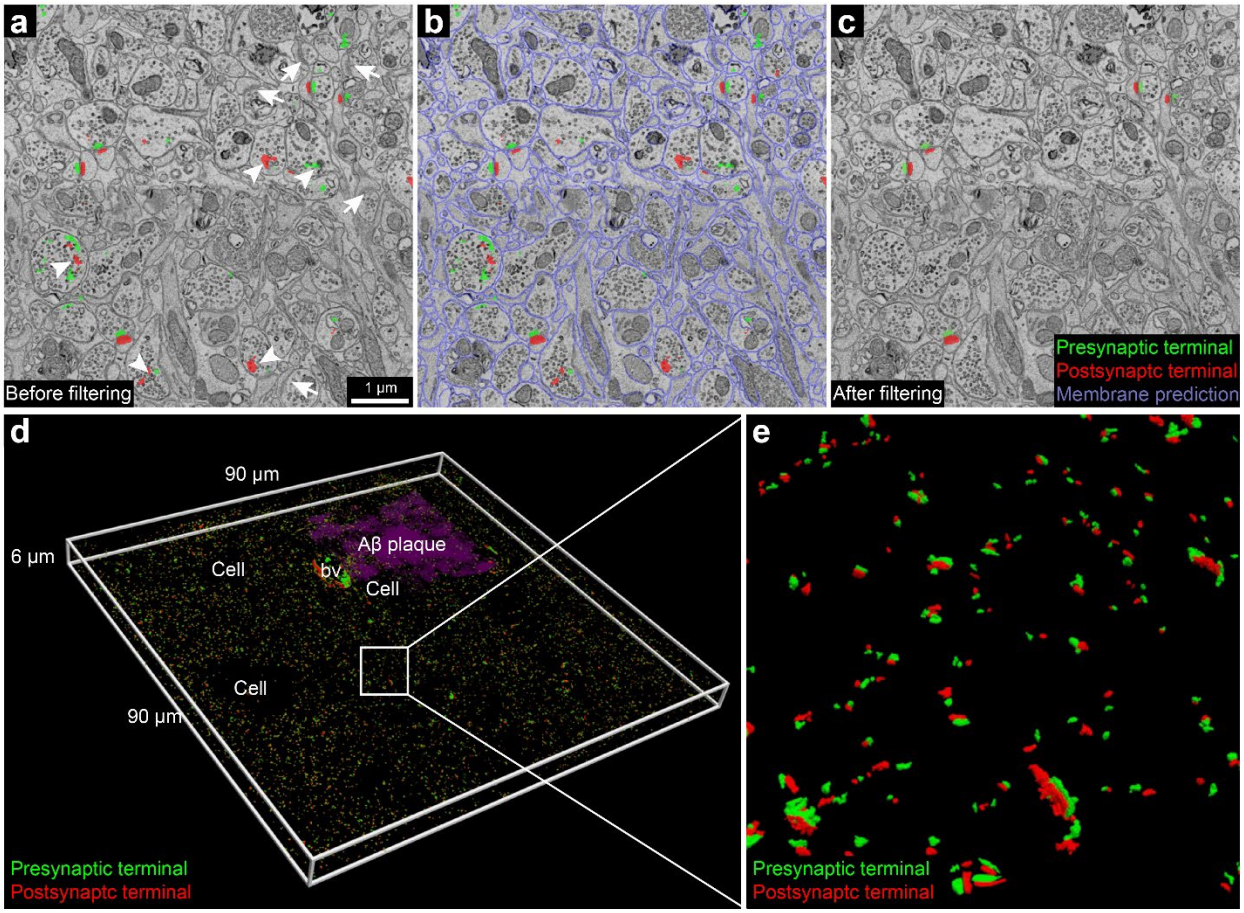

Figure 9. Synapse detection results using a U-Net classifier based on (Çiçek et al., 2016).

a, Synapses detected in a region of neuropil before filtering. Arrows, synapses that were missed by the detection. Arrowheads, false positive detections within neuronal processes. **b**, Synapses detected before filtering shown together with 2D membrane prediction. **c**, Synapse detected after filtering through membrane prediction. **d**, 3D rendering of all detected synapses in a box with the dimensions of 90 µm x 90 µm x 6 µm where there was an Aβ plaque, a blood vessel and several cell bodies. The Aβ plaque is the same one as in Figure 8 a. **d**, Enlarged boxed inset from **c**.

To improve the accuracy of the synapse detection for further analysis, we used the another machine learning approach implemented in PyTorch (Lin et al., 2021) to detect synapses in boxes of the small-scale dimensions. At three distances (10 µm, 20 µm, 30 µm) from the center of an Aβ plaque, we randomly picked three small boxes with the dimensions of 6 µm x 6 µm x 6 µm and eliminated boxes that were contaminated by blood vessel or cell bodies (see Sup. Figure 4). By applying PyTorch synapse detection on one of the boxes, we obtained a more precise evaluation of synapse density (precision of 86.06% and a recall of 98.88%) at different distances.

Synapse detection on all nine boxes (Figure 10 a, b, c) showed that a decrease in synapse density as regions progressively closer to the plaque: synapse density was 0.181 ± 0.068 per μm³ at 10 μm, 0.653 ± 0.025 per μm³ at 20 μm, 1.216 ± 0.174 per μm³ at 30 μm (Figure 10 d). There was a statistically significant trend as the distance to the plaques dropped from 30 μm to 10 μm (two-tailed, unpaired t-test. 10 μm vs. 20 μm, $p = 0.0004$; 20 μm vs. 30 μm, $p = 0.0051$; 10 μm vs. 30 μm, $p = 0.0007$).

The average synapse volume (pre-synaptic side) was 0.00436 ± 0.00007 μm³ at 10 μm, 0.00452 ± 0.00030 μm³ at 20 μm, 0.00476 ± 0.00071 μm³ at 30 μm (Figure 10 e). There was no statistically significant change in average synapse volume as the distance to the plaques dropped from 30 μm to 10 μm (two-tailed, unpaired t-test. 10 μm vs. 20 μm, $p = 0.4356$; 20 μm vs. 30 μm, $p = 0.6104$; 10 μm vs. 30 μm, $p = 0.3864$).

The total synaptic volume (pre-synaptic side) for each was 0.170 ± 0.065 μm³ at 10 μm, 0.638 ± 0.066 μm³ at 20 μm, 1.255 ± 0.282 μm³ at 30 μm (Figure 9 f). There was a statistically significant decrease in total synaptic volume as the distance to the plaques dropped from 30 μm to 10 μm (two-tailed, unpaired t-test. 10 μm vs. 20 μm, $p = 0.0009$; 20 μm vs. 30 μm, $p = 0.0210$; 10 μm vs. 30 μm, $p = 0.0029$).

We plotted the frequency distributions of synapse volumes (pre-synaptic + post-synaptic, Figure 11 a; pre-synaptic, Sup. Figure 5 a; post-synaptic, Sup. Figure 5 b) for all nine boxes. We found that the pre-synaptic volumes of all boxes were slightly larger than the post-synaptic volumes (Sup. Figure 5 c). To test if smaller or larger synapses were prone to be eliminated when closer to the plaque, we combined the synapse volume (pre-synaptic + post-synaptic) data of the three boxes at each distance and plotted the frequency distributions again (Figure 11 b). We performed two-sample Kolmogorov–Smirnov tests and found there was no significant difference between any two of the distributions (10 μm vs. 20 μm: $p = 0.8498$; 20 μm vs. 30 μm: $p = 0.1231$; 10 μm vs. 30 μm: $p = 0.09247$). This result suggests that there was synapse elimination closer to the plaque, but the elimination did not preferentially target smaller nor larger synapses. Synapses of all volumes were possibly eliminated equally when closer to the plaque.

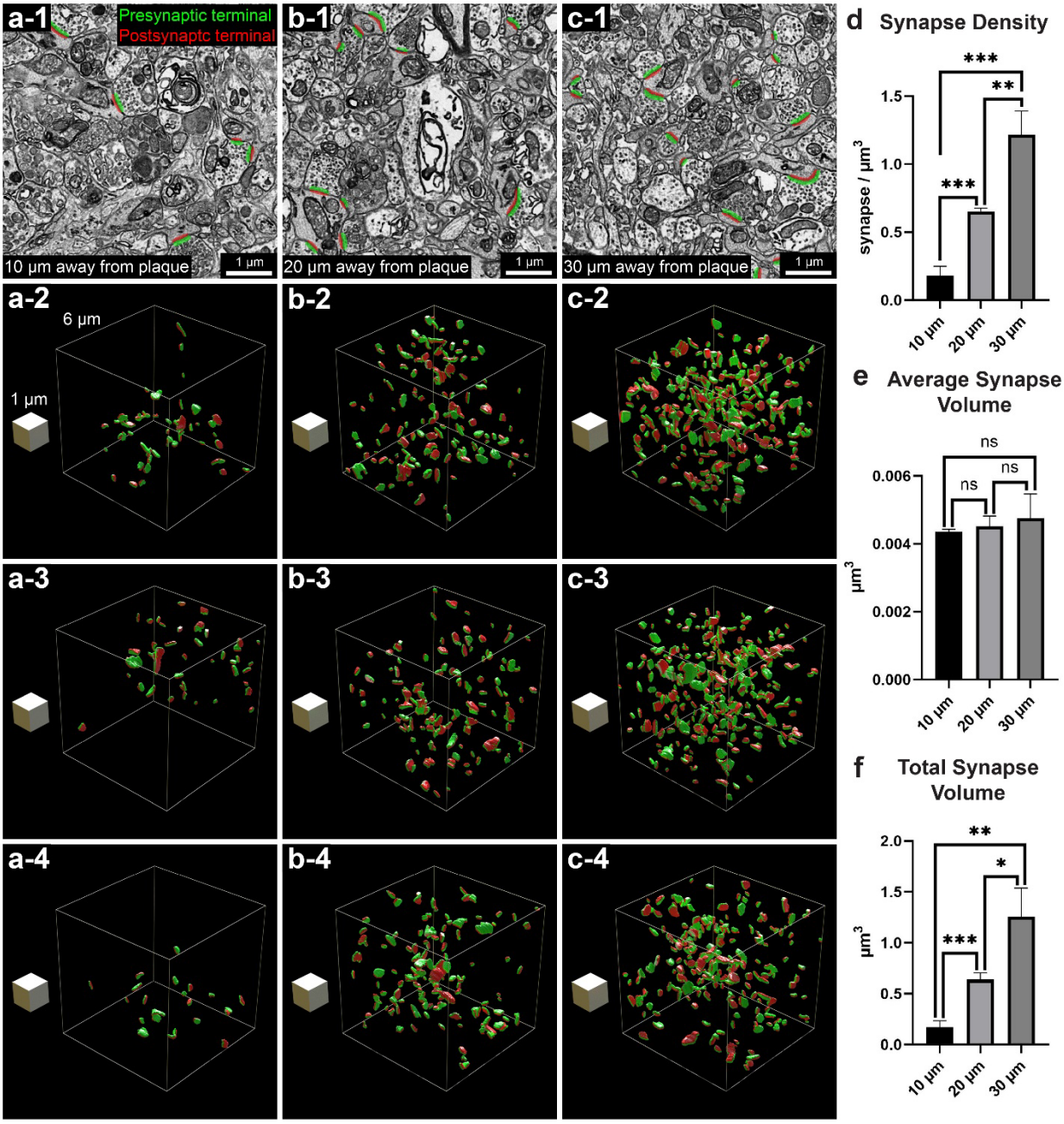

Figure 10. Synapse detection results using PyTorch (Lin et al., 2021)**.**

a-1, A representative image slice with detected synapses from the box at 10 μm away from the center of an Aβ plaque. **a-2** to **a-4**, 3D rendering of all detected synapses in the box as in **a-1** with the dimensions of 6 μm x 6 μm x 6 μm at 10 μm away from the center of an Aβ plaque. White block is of the dimension of 1 μm x 1 μm x 1 μm. **b-1**, A representative image slice with detected synapses from the box at 20 μm away from the center of an Aβ plaque. The image slice is of the dimension of 6 μm x 6 μm. **b-2** to **b-4**, 3D rendering of all detected synapses in the box as in **b-1** with the dimensions of 6 μm x 6 μm x 6 μm at 20 μm away from the center of an Aβ plaque. White block is of the dimension of 1 μm x 1 μm x 1 μm. **c-1**, A representative image slice with detected synapses from the box at 30 μm away from the center of an Aβ plaque. The image slice is of the dimension of 6 μm x 6 μm. **c-2** to **c-4**, 3D rendering of all detected synapses in the box as in **c-1** with the dimensions of 6 μm x 6 μm x 6 μm at 30 μm away from the center

of an Aβ plaque. White block is of the dimension of 1 μm x 1 μm x 1 μm. **d**, Synapse density, **e**, Average synapse volume, **f**, Total synapse volume were measured for each of the three box at 10 μm away from the plaque, the three box at 20 μm away from the plaque, and the three box at 30 μm away from the plaque. Two-tailed, unpaired t-test was performed. Synapse density, 10 μm vs. 20 μm, p = 0.0004, t=11.29, df=4; 20 μm vs. 30 μm, p = 0.0051, t=5.553, df=4; 10 μm vs. 30 μm, p = 0.0007, t=9.597, df=4. Average synapse volume, 10 μm vs. 20 μm, p = 0.4356, t=0.8655, df=4; 20 μm vs. 30 μm, p = 0.6104, t=0.5519, df=4; 10 μm vs. 30 μm, p = 0.3864, t=0.9713, df=4. Total synapse volume, 10 μm vs. 20 μm, 0.0009, t=8.789, df=4; 20 μm vs. 30 μm, p = 0.0210, t=3.690, df=4; 10 μm vs. 30 μm, p = 0.0029, t=6.489, df=4.

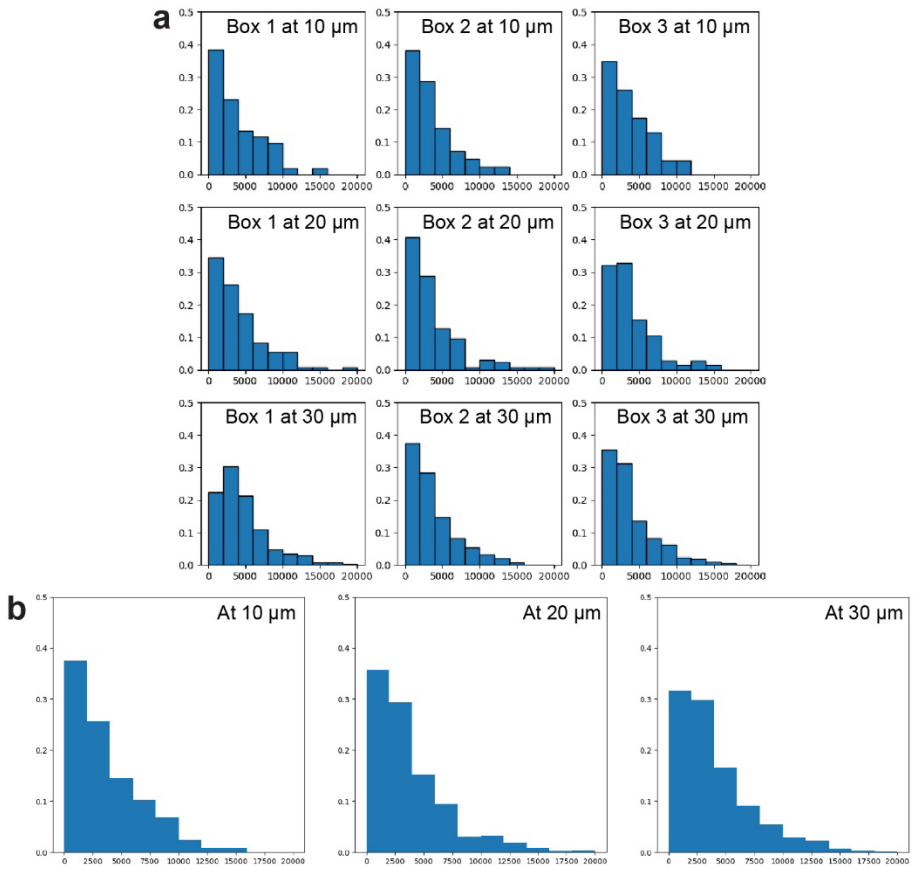

Figure 11. Frequency distributions of the synapse volume (pre-synaptic + post-synaptic).

a, Frequency distributions of synapses volumes (pre-synaptic + post-synaptic) of the nine boxes at 10 μm away, 20 μm away, and 30 μm away from the plaque. Synapse volume is shown in the unit of voxels. Each voxel equals 0.0000192 μm^3. **b**, Combined frequency distributions of synapses volumes (pre-synaptic + post-synaptic) at 10 μm away, 20 μm away, and 30 μm away from the plaque.

Conclusions and discussion

Here we report a new vCLEM technique enabled by fluorescent nanobody immunolabeling probes to localize three AD-related molecules (pTau, Aβ, CD11b as microglial marker) in a large volume connectomics dataset. This work demonstrates that fluorescent labeling of the target molecules can

easily be superimposed with excellent ultrastructure in vEM datasets by omitting detergents in the immunolabeling step. We identified several intracellular and extracellular abnormalities associated with the recognized target molecules. We performed automatic segmentation, and semi-automatic 3D reconstruction of neurons, indicating that this approach enables connectomics analysis of a neurological disease model. We also performed machine-learning-based automatic synapse detection, which uncovered significant alterations in synapse density and total synapse volume related to the location of an Aβ plaque. We made this vCLEM dataset publicly accessible by this link to allow researchers interested in AD to look for other abnormalities associated with the localization of pTau and Aβ. This approach could also be used to localize other molecular abnormalities in large-volume connectomics datasets from AD animal or human patient samples.

We discovered two novel abnormalities at the AIS of pyramidal neurons associated with Alzheimer's proteins. One is a swelling filled with pTau at the AIS of a pyramidal neuron with pTau labeling in its cell body (Figure 5 h-1, h-2; Figure 8 b). The other abnormality are the enlarged blebs filled with pTau at the AIS of pyramidal neurons with pTau labeling in its cell body (Figure 5 g-1, g-2; Figure 8 c). We also observed spines at the AIS of some other pyramidal neurons in our datasets, which did not have the anti-pTau labeling, nor were they abnormally enlarged. Interestingly, in the vEM dataset generated from the human cortex (Shapson-Coe et al., 2021), there were also normal looking spines at the AIS of some pyramidal neurons. The abnormalities in this mouse dataset may be attributed to perturbations of molecular mechanisms at the AIS by pTau and Aβ. When the membrane protein ankyrin-G was depleted from the AIS, the AIS developed ectopic spines that contain excitatory postsynaptic components (Sobotzik et al., 2009). The AIS also functions as a barrier that regulates the anterograde and retrograde flow of tau proteins (X. Li et al., 2011). Depletion of ankyrin-G or contact with Aβ disrupts this diffusion barrier (Zempel et al., 2017). A possible mechanism that could give rise to these abnormalities is that the AIS is targeted by pTau or Aβ from nearby plaque material, disrupting the molecular mechanism that involves ankyrin-G and causing failure of tau sorting. This could plausibly lead to swelling and abnormally enlarged spines at the AIS that retain the missorted pTau. Because pTau can aggregate in spines (Blazquez-Llorca et al., 2011), the enlarged spine heads with high capacitance and high resistance skinny necks may attenuate the synaptic signal and prevent it from reaching the axon. As

a result, despite their location these spines may be less likely to excite the axon.

Automatic synapse detection showed a decrease in synapse density and total synapse volume as the distance to the Aβ plaque decreased. Several previous studies on human (Adams, 1987; S. W. Scheff et al., 1990) or AD mouse models (Hillman & Chen, 1981) showed that sizes of synaptic contacts in AD tissue samples were substantially larger compared to controls. A compensatory mechanism was proposed: as synapse density decreases, synapse size grows larger (S. W. Scheff & Price, 1993). The decrease in synapse density may be caused by Aβ's synaptic toxicity (Hampel et al., 2021; Koffie et al., 2009; Lue et al., 1999; Mucke et al., 2000; Urbanc et al., 2002) and/or mediated by glial mechanisms (Chung et al., 2015; Rajendran & Paolicelli, 2018; Vilalta & Brown, 2018) as we observed an increased number of glial processes from reactive microglia and astrocytes nearby Aβ plaques (Figure 4, Figure 7 b, also see Sup. Figure 6 for astrocytic processes). A compensatory mechanism is less likely to account for our result because we did not observe an increase in average synapse volume but rather a decrease in total synapse volume.

In the future, by expanding the panel of fluorescent nanobody probes, or by combining it with other types of immunolabeling compatible with vCLEM, this approach will become more powerful for the localization of abnormal protein depositions in AD and other neurodegenerative diseases. For example, nanobody probes for different Aβ species (e.g. Aβ1-40 and Aβ1-42) or Aβ with different conformations (e.g. oligomers, protofibrils, and fibrils) (Hampel et al., 2021) and for tau isoforms or tau with site-specific phosphorylation (Arendt et al., 2016) will be useful because these molecules present more severe or specific forms of toxicity to neurons or synapses in AD (Arendt et al., 2016; Cline et al., 2018; Habicht et al., 2007; Hampel et al., 2021). Nanobody probes for other neurodegeneration-related molecules (e.g. α-synuclein, TDP-43, and huntingtin) (Bates et al., 2015; Taylor et al., 2002; Twohig & Nielsen, 2019; Wilson et al., 2011) could allow this approach to be used for other types of neurodegenerative diseases such as Parkinson's disease, Frontotemporal Dementia, and Huntington's disease. There are already nanobodies for these molecules developed for other purposes (Danis et al., 2022; De Genst et al., 2010; Habicht et al., 2007; Lafaye et al., 2009) that can easily be converted to fluorescent probes.

Of course, the same approach can be used to probe a variety of other proteins including cell type specific markers. The pathological proteins studied here are selectively associated with different types of

cells such as glial cells and subtypes of inhibitory neurons (Hattori et al., 2017; Kahlson & Colodner, 2015). So nanobodies or other types of affinity reagents that can be used in detergent-free immunolabeling (such as single-chain variable fragments) specific for markers of particular cell types (Han et al., 2023) could be included to explore how toxic molecules specifically impair certain cell types. Special sample preparation methods (Fulton & Briggman, 2021; Lu et al., 2023) that allow full-length antibodies to be used in detergent-free immunolabeling can also be combined with our technique to expand the list of markers that can be labeled.

Recent large-scale proteomic and transcriptomic studies (Johnson et al., 2022, 2020; Magistri et al., 2015; Mathys et al., 2019) have showed alterations at the levels of protein and gene expression in AD. To localize these new molecular abnormalities in connectomics datasets, a large collection of nanobody probes that target common molecular markers will be needed. Multiple nanobody databases are now available where thousands of nanobody sequences are being deposited (Deszyński et al., 2021; Wilton et al., 2018). Researchers can query sequences of nanobodies that target the molecular abnormalities of interest, and then, as we have done, convert these nanobodies into fluorescent probes. If no nanobody for a desired target is available, there are efficient ways to generate new nanobodies from immune libraries (Muyldermans, 2021) or synthetic libraries (McMahon et al., 2018; Zimmermann et al., 2020). With a growing collection of nanobody probes, the combination of this technique with super-multicolor fluorescence imaging enabled by spectral unmixing (Seo et al., 2022) or multiplexed Raman vibrational imaging (Wei et al., 2017) is a desirable goal, in order to achieve simultaneous multiplexed labeling of many probes in the same sample.

This technique can be applied on human samples to study this disease in situ. Because immunolabeling for a specific molecule does not require the use of transgenic animals, human samples are appropriate targets. So as long as the nanobody probe can bind to the molecule-of-interest in human tissues, it can be used to localize this molecule. The two nanobody probes (A2 and R3VQ) tested in this study detect their targets in brain samples from AD patients (T. Li et al., 2016). Our technique could thus be used to apply these nanobodies to postmortem or surgical samples from AD patients. A new method to process large surgical brain samples from patients with neurological disorders for vEM was recently described (Karlupia et al., 2023; Loomba et al., 2022). It is possible to combine this method with

nanobody labeling to investigate the connectomics of AD patients' brain samples.

Material and methods

Animals

Animals used in the study were female one-year old 3xTg (B6;129-Tg(APPSwe,tauP301L)1Lfa Psen1$^{tm1Mpm/Mmjax}$) mice (Jackson Laboratory) and female one-year old B6129SF2/J mice (as age-matched control animal, Jackson Laboratory). All experiments using animals were conducted according to US National Institutes of Health guidelines and approved by the Committee on Animal Care at Harvard University.

Nanobody production

A signal peptide (MDWTWRILFLVAAATGAHS) was added to the N'-terminus of the nanobody. A sortase tag (SLPETGG) and a 6 x His tag was added to the C'-terminus. The amino acid sequence was reverse translated into a DNA sequence with codon optimization for human cells. The DNA sequence was synthesized and cloned into pcDNA 3.1 vectors.

Nanobody expression was performed with Expi 293 cells (ThermoFisher). Detailed expression and purification protocols can be found in (Han et al., 2023).

Sortase reaction

The production of GGGC-dye conjugates was performed as described in (Han et al., 2023). The sortase reaction was performed as described in (Antos et al., 2017; Han et al., 2023).

Perfusion and fixation

The mouse was anesthetized by isoflurane until there was no toe-pinch reflex. Mice were then transcardially perfused with aCSF (125 mM NaCl, 26 mM $NaHCO_3$, 1.25 mM NaH_2PO_4, 2.5 mM KCl, 26 mM glucose, 1 mM $MgCl_2$ and 2 mM $CaCl_2$ (all chemicals from Sigma-Aldrich) at the flow rate of 10 ml/min for 2 min to remove blood, followed with 4% paraformaldehyde (Electron Microscopy Sciences), 0.1% glutaraldehyde (Electron Microscopy Sciences) in 1 x PBS for 3 min for fixation. Brains were dissected and then post-fixed in the same fixative on a rotator overnight at 4°C. Brains were sectioned into 50-μm or 120-μm coronal sections using a Leica VT1000 S vibratome and stored in the same fixative

at 4°C.

Immunofluorescence

Detergent-free immunofluorescence labeling was performed with nanobody probes (see Sup. Table 1 for the nanobody probes and the final concentration of each nanobody probe used in this study). The detailed protocol was described in (Fang et al., 2018; Han et al., 2023). For the 120-μm coronal sections used for vCLEM, the section was first washed with 1 x PBS for 3 x 10 min, and then blocked in glycine blocking buffer (0.1 M glycine, 0.05% NaN_3 in 1 x PBS) for 1 h on a rotator at 4 °C. The labeling solution was prepared by diluting nanobody-dye conjugates in glycine blocking buffer (see Sup. Table 1 for the final concentration used). The labeling solution and any remaining steps were protected from light. The section was incubated with the labeling solution on a rotator at 4 °C for three to seven days. The 120-μm sections for Figure 2 were first incubated with the labeling solution with only the anti-pTau nanobody for three days, and then incubated with the labeling solution with the anti-Aβ and the anti-CD11b nanobodies for another three days. The 120-μm section for Figure 3 was incubated with the labeling solution with all four nanobodies for seven days. After the incubation, the section was washed with 1 x PBS for 3 x 10 min, and then stained with Hoechst 33342 (Invitrogen, diluted 1:5000 in 1 x PBS) for 1 h on a rotator at 4 °C. The section was washed with 1 x PBS for 3 x 10 min, and then mounted onto glass slide (VWR).

To validate the labeling of the nanobody A2, double immunofluorescence labeling with detergent was performed on 50-μm sections with the anti-pTau mAb AT8 (ThermoFisher) plus the anti-mouse IgG H + L secondary antibody conjugated with Alexa Fluor 488 (ThermoFisher), and A2 conjugated with Alexa Fluor 594 (see Sup. Figure 1 a) (see Sup. Table 2 and 3 for the final concentrations used for each probe). To validate the labeling of the nanobody R3VQ, double immunofluorescence labeling with detergent was performed with the anti-Aβ mAb 4G8 conjugated with Alexa Fluor 647 (BioLegend) and R3VQ conjugated with 5-TAMRA (see Sup. Figure 2) (see Sup. Table 2 and 3 for the final concentrations used for each probe). The detailed protocol is available on the NeuroMab website (*Immunofluorescence Labeling of Free-Floating Perfusion-Fixed Brain Sections*, 2016). In brief, 50-μm coronal sections were first washed with 1 x PBS for 3 x 10 min, and then blocked in vehicle (10% normal goat serum, 0.3% Triton X-100 in 1 x PBS) overnight on a rotator at 4 °C. Subsequent steps were protected from light. For the experiment

with AT8 and A2, the sections were then incubated with primary antibody solution plus nanobody probes overnight on a rotator at 4 °C. After the incubation, sections were washed with vehicle for 3 x 10 min, and then incubated with the secondary antibody solution for 1 hour on a rotator at 4 °C. For the experiment with 4G8 and R3VQ, the sections were then incubated with primary antibody solution plus nanobody probes for 3 days on a rotator at 4 °C. After the incubation, sections were washed with 1 x PBS for 3 x 10 min, and then stained with Hoechst (diluted 1:5000 in 1 x PBS) for 1 h on a rotator at 4 °C. Sections were washed with 1 x PBS for 3 x 10 min, and then mounted onto glass slides.

Fluorescence confocal microscopy

Fluorescence confocal microscopy was performed as described in (Han et al., 2023). In brief, 50-µm sections were mounted in Vectashield H-1000 (Vector Laboratories) with a #1 coverslip (Electron Microscopy Sciences) on top sealed with clear nail polish. 120-µm sections (for vCLEM) were mounted in 1 x PBS inside 120-um spacer (Invitrogen) with a #1 coverslip on top sealed with the spacer. Sections were imaged with a Zeiss LSM 880 confocal laser scanning microscope equipped with either a 20x/0.8 NA air-objective or a 40x/1.1 NA water immersion objective. The 120-µm section for vCLEM was imaged with a 40x/1.1 NA water immersion objective. Acquisition of double or triple color fluorescent images was done with appropriate band pass filters for the specific fluorescent dyes to avoid crosstalk.

The brightness, contrast, and gamma of all fluorescent images were adjusted. Fluorescence image volumes were projected to a single plane by maximum intensity for visualization in 2D.

EM preparation

Sample preparation for electron microscopy was performed as described in (Han et al., 2023). After the 120-µm sections was imaged, it was transferred into 3.7 ml shell vials with 1 ml secondary fixative (2% PFA, 2,5% glutaraldehyde in 0.15M sodium cacodylate buffer with 4mM Ca^{2+} and 0.4 mM Mg^{2+}) and incubated for at least one week on a rotator at 4 °C. A modified ROTO (Reduced Osmium-Thiocarbohydrazide-Osmium) protocol was used to stain the section. The section was embedded in LX-112 resin.

X-ray microCT scanning

X-ray micro-computed tomography (µCT) images of the resin-embedded sections were acquired

using a Zeiss Xradia 510 Versa system and Zeiss' Scout and Scan software. Detailed protocol was described in (Han et al., 2023).

EM imaging

The resin-embedded sections were cut into 30 nm serial ultrathin sections using automated tape-collecting ultramicrotome (ATUM) (Kasthuri et al., 2015). Serial sections were collected onto carbon-coated and plasma-treated Kapton tape. The tape was cut into strips and affixed onto 150 mm silicon wafers (University Wafer). A Zeiss Sigma scanning electron microscope was used to acquire overview images from the serial sections. Detailed protocol was described in (Han et al., 2023).

Prior to acquiring high-resolution images, the serial section sections on wafers were post-stained for 4 min with a 3% lead citrate solution. After staining, the sections were degassed for a minimum of 24 h at 1x10-6 Torr. A Zeiss MultiSEM 505 scanning electron microscope equipped with 61 electron beams was used to acquire high-resolution images from the serial sections. Images were collected using a 1.5-kV landing energy, 4-nm image pixel, and a 400-ns dwell time.

High-resolution EM image processing

The preparation of the vEM data before it could be segmented/analyzed includes two steps: affine stitching and elastic alignment. Detailed protocol was described in (Han et al., 2023). We excluded 20 slices that had sub-optimal imaging quality (e.g. very thin slices or contains tears and wrinkles) and copied the adjacent sections in the places of these excluded slices. The aligned stack was rendered at full resolution (4 x 4 x 30 nm) and each section was cut into 4k x 4k .png tiles, imported into VAST as a .vsvi file, and ingested into Neuroglancer for further analysis.

The initial alignment of the vEM dataset showed several jumps through the z-axis. A second attempt at alignment was performed after discarding four more slices (we also copied the adjacent sections in the places of these discarded slices) that had suboptimal image quality, which successfully eliminated the jumps. The 3D reconstruction of Neuron 3, the automatic Aβ plaque detection, and the synapse detection using a U-Net classifier was performed on the first version of alignment. The 3D reconstruction of Neuron 3 and the automatic Aβ plaque detection were later transferred to the second version of the alignment based on matching coordinates. The other reconstructions and the synapse detection by PyTorch were performed on the second version of the alignment. The publicly accessible

vCLEM dataset shows the second version of the alignment.

Co-registration of fluorescence and EM volumes

The co-registration was performed using the BigWarp plugin in FIJI. Detailed description can be found in (Han et al., 2023).

Automatic segmentation

We segmented a central cutout of the dataset using flood-filling networks (FFNs, Januszewski 2018). The FFN segmentation model was trained at 16 x 16 x 30 nm resolution on the H01 dataset (Shapson-Coe et al., 2021), and run here on CLAHE intensity normalized data (Zuiderveld, 1994) downsampled to match the trained model resolution. But direct application of the h01-trained FFN to the Alzheimer's dataset did not perform well. Therefore we used Segmentation Enhanced CycleGAN (Michal Januszewski & Jain, 2019) to modify the visual appearance of the Alzheimer's dataset at 16 x 16 x 30 nm to mimic h01, prior to running the FFN. The resulting segmentation can be explored in Neuroglancer.

2D membrane detection at 4 x 4 x 30 nm resolution was performed on the vEM dataset using a method developed in our lab. A description of this approach was given in (Karlupia et al., 2023; Meirovitch et al., 2018; Pavarino et al., 2023). In brief, an algorithm (Pavarino et al., 2023) pre-trained on a mouse cerebellar dataset was used to generate 2D membrane detection.

Automatic Aβ plaque segmentation

We optimized a DeepLab-v3 semantic segmentation model (L.-C. Chen et al., 2018) on a cropped stack of images with manually identified Aβ plaque. The model was pre-trained on another vEM dataset from the Alzheimer's disease mouse model Tg2576 (Dr. Olga Morozova, personal communication) to decrease the requirements of manually annotated training data in the target volume. We also oversample patches near the Aβ plaque border during training to improve segmentation quality as the mask structures in those patches are more challenging. The training and inference are implemented with the open-source PyTorch Connectomics codebase (Lin et al., 2021).

Synapse detection using a U-Net classifier and subsequent filtering

The synapse model was a three-stage U-Net architecture with an initial feature size of 32 and scaled 2x for each stage of the U-Net. Model output was volumetric, with the output stage a 3-class

softmax classifier with classes background, pre-synaptic site, and post-synaptic site. During training labels were weighted 2x, 2x, and 1x for pre/post and background, respectively. A stronger positive weight was imposed in an effort to bias the network towards a higher recall value at the expense of potentially more false positives, as there are downstream filtering heuristics applied that eliminate non-plausible pre/post pairs, e.g. a synapse predicted on the boundary of a nucleus, wholly contained within a segmented neuron.

Training data consisted of 6x ROIs from a previously-annotated human dataset (Shapson-Coe et al., 2021), sized 8 x 8 x 100 µm (1k*1k*100 voxels) with densely annotated pre/post volumetric labels for a total of 3824 unique synapses. Examples were generated at the centroid of each pre- and post-synaptic site, and augmentation was performed by applying an offset to the centroid location by up to 27 x 27 x 3 voxels In XYZ. Further augmentation included permutation of X and Y axes and reflections along X, Y, and Z axes. Due to the size of the network, the model was trained at a batch size of 1, and was trained for a total of 51M steps. Inference was performed on the entire dataset.

We filter synapse annotations using three criteria: size, proximity to a membrane, and presence of adjacent pre- and postsynaptic annotations. The minimum size of an annotation is 60 voxels, and membranes are dilated using a disk of radius 4 prior to filtering annotations based on overlap with membrane voxels. For pre- and post- synapse annotation filtering, all pre- and post- synaptic annotations remaining have at least one partner of the opposite type within 30 pixels in x and y and 3 slices in z. This distance is determined via centroids. One additional constraint for pre- and post- synaptic partners is that the volume of candidate partners must differ by less than a factor of 2. The resulting annotations have little to no noise in the cytoplasm.

Synapse detection using the PyTorch Connectomics Package (Lin et al., 2021)

We sampled nine EM image subvolumes with dimensions of 6 µm x 6 µm x 6 µm at three distances (10 µm, 20 µm, 30 µm) from the center of an Aβ plaque at the original resolution. We took a semi-automatic approach to annotate all the synapses in these subvolumes. First, one human annotator labeled all the pre- and post-synaptic appositions in 1/4 of one of the nine EM image subvolumes. Then, we trained a synapse detection model (Parag et al., 2019) using the manual annotations with the PyTorch Connectomics deep learning package. To refine the model, we tested it on all slices of this subvolume,

manually proofread its results, and fine-tuned the model with all the annotations, which led to a desirable detection accuracy and recall result. Lastly, we used the improved model to detect synapses in the remaining eight subvolumes and proofread the automatic predictions.

Statistical analysis

Two-tailed, unpaired t-tests on synaptic density, synaptic volume and total synaptic volume of the three categories defined in the section of synapse detection (The PyTorch method) were performed in Prism-GraphPad. Two-sample Kolmogorov–Smirnov test was performed using Python.

Acknowledgement

We thank the Harvard Center for Biological Imaging (RRID:SCR_018673) for infrastructure and support, the Biopolymers and Proteomics Core Facility at the Koch Institute at MIT for processing the peptide-fluorescent dye conjugates, the Bauer Core Facility at Harvard for infrastructure and support, Dr. Olga Morozova for helpful discussion on the Alzheimer's disease mouse model and immunolabeling of Aβ plaques, Dr. Tao Fang and Dr. Xiaotang Lu for helpful discussion on nanobody production, and Dr. Marta Montero-Crespo for helpful discussion on synapse annotation. This work was supported by NIH grants U19 NS104653, UG3 MH123386, and P50 MH094271 (J. W. L.); NSF grants NSF-CAREER-2239688 (D. W.), NCS-FO-2124179, and NCS-FO-1835231 (H. Pfister.), NLM T15LM007092-31 (M. S.); Office of Naval Research grant N00014-20-1-2828 (J. W. L). X. H. was supported by the Edward R. and Anne G. Lefler predoctoral fellowship from the Lefler Center for Neurodegenerative Disorders at Harvard Medical School and the Simmons Awards from the Harvard Center for Biological Imaging.

Author Contribution

X. H. and J. W. L conceived this study. Nanobody A2 and R3VQ were originally generated in the labs of P. L., S. B., and B. D.. X. H. generated the fluorescent nanobody probes A2 and R3VQ. H. Ploegh provided the fluorescent anti-CD11b, anti-GFAP, and anti-Ly6C/6G nanobodies. X. H. performed the LM experiments. X. H. and R. S. performed the EM experiments. S. W. performed the imaging processing of the vEM dataset. P. H. L. and V. J. performed 3D segmentation and curated the vCLEM dataset at

Neuroglancer. X. H., M. S., and F. A. performed 3D reconstruction of neurons. T. B. performed synapse detection using a U-Net classifier. Y. M. (yaron.mr@gmail.com) performed 2D membrane detection. M. S. performed the filtering of the synapse detection results using a U-Net classifier. S. A., D. W., and X. H. performed synapse detection using PyTorch and associated analysis. Z. L., and H. Pfister performed automatic plaque detection. D. B. provided the reconstruction tool VAST and advice on 3D reconstruction and rendering. Y. W. helped with LM and EM co-registration. X. H. and J. W. L wrote the paper with inputs from H. Ploegh, B. D., D. B., and R. S.

Competing interests

The authors declare no competing interests.

References

Adams, I. (1987). Plasticity of the synaptic contact zone following loss of synapses in the cerebral cortex of aging humans. *Brain Research*, *424*(2), 343–351.

Antos, J. M., Ingram, J., Fang, T., Pishesha, N., Truttmann, M. C., & Ploegh, H. L. (2017). Site-Specific Protein Labeling via Sortase-Mediated Transpeptidation. In *Current Protocols in Protein Science* (Vol. 89, Issue 1). https://doi.org/10.1002/cpps.38

Arendt, T., Stieler, J. T., & Holzer, M. (2016). Tau and tauopathies. *Brain Research Bulletin*, *126*(Pt 3), 238–292.

Barbone, G. E., Bravin, A., Mittone, A., Pacureanu, A., Mascio, G., Di Pietro, P., Kraiger, M. J., Eckermann, M., Romano, M., Hrabě de Angelis, M., Cloetens, P., Bruno, V., Battaglia, G., & Coan, P. (2022). X-ray multiscale 3D neuroimaging to quantify cellular aging and neurodegeneration postmortem in a model of Alzheimer's disease. *European Journal of Nuclear Medicine and Molecular Imaging*, *49*(13), 4338–4357.

Bates, G. P., Dorsey, R., Gusella, J. F., Hayden, M. R., Kay, C., Leavitt, B. R., Nance, M., Ross, C. A., Scahill, R. I., Wetzel, R., Wild, E. J., & Tabrizi, S. J. (2015). Huntington disease. *Nature Reviews. Disease Primers*, *1*, 15005.

Belfiore, R., Rodin, A., Ferreira, E., Velazquez, R., Branca, C., Caccamo, A., & Oddo, S. (2019). Temporal and regional progression of Alzheimer's disease-like pathology in 3xTg-AD mice. *Aging Cell*, *18*(1), e12873.

Bisht, K., Sharma, K. P., Lecours, C., Sánchez, M. G., El Hajj, H., Milior, G., Olmos-Alonso, A., Gómez-Nicola, D., Luheshi, G., Vallières, L., Branchi, I., Maggi, L., Limatola, C., Butovsky, O., & Tremblay, M.-È. (2016). Dark microglia: A new phenotype predominantly associated with pathological states. *Glia*, *64*(5), 826–839.

Blazquez-Llorca, L., Garcia-Marin, V., Merino-Serrais, P., Ávila, J., & DeFelipe, J. (2011). Abnormal tau phosphorylation in the thorny excrescences of CA3 hippocampal neurons in patients with Alzheimer's disease. *Journal of Alzheimer's Disease: JAD*, *26*(4), 683–698.

Blazquez-Llorca, L., Merchán-Pérez, Á., Rodríguez, J.-R., Gascón, J., & DeFelipe, J. (2013). FIB/SEM technology and Alzheimer's disease: three-dimensional analysis of human cortical synapses. *Journal of Alzheimer's Disease: JAD*, *34*(4), 995–1013.

Bogovic, J. A., Hanslovsky, P., Wong, A., & Saalfeld, S. (2016). Robust registration of calcium images by learned contrast synthesis. *2016 IEEE 13th International Symposium on Biomedical Imaging (ISBI)*, 1123–1126.

Buhmann, J., Sheridan, A., Malin-Mayor, C., Schlegel, P., Gerhard, S., Kazimiers, T., Krause, R., Nguyen, T. M., Heinrich, L., Lee, W.-C. A., Wilson, R., Saalfeld, S., Jefferis, G. S. X. E., Bock, D. D., Turaga, S. C., Cook, M., & Funke, J. (2021). Automatic detection of synaptic partners in a whole-brain Drosophila electron microscopy data set. *Nature Methods*, *18*(7), 771–774.

Chen, G.-F., Xu, T.-H., Yan, Y., Zhou, Y.-R., Jiang, Y., Melcher, K., & Xu, H. E. (2017). Amyloid beta: structure, biology and structure-based therapeutic development. *Acta Pharmacologica Sinica*, *38*(9), 1205–1235.

Chen, L.-C., Zhu, Y., Papandreou, G., Schroff, F., & Adam, H. (2018). Encoder-decoder with atrous separable convolution for semantic image segmentation. In *Computer Vision – ECCV 2018* (pp. 833–851). Springer International Publishing.

Chung, W.-S., Welsh, C. A., Barres, B. A., & Stevens, B. (2015). Do glia drive synaptic and cognitive impairment in disease? *Nature Neuroscience*, *18*(11), 1539–1545.

Çiçek, Ö., Abdulkadir, A., Lienkamp, S. S., Brox, T., & Ronneberger, O. (2016). 3D U-Net: Learning Dense Volumetric Segmentation from Sparse Annotation. *Medical Image Computing and Computer-Assisted Intervention – MICCAI 2016*, 424–432.

Cline, E. N., Bicca, M. A., Viola, K. L., & Klein, W. L. (2018). The Amyloid-β Oligomer Hypothesis: Beginning of the Third Decade. *Journal of Alzheimer's Disease: JAD*, *64*(s1), S567–S610.

Crowther, R. A. (1991). Straight and paired helical filaments in Alzheimer disease have a common structural unit. *Proceedings of the National Academy of Sciences of the United States of America*, *88*(6), 2288–2292.

Danis, C., Dupré, E., Zejneli, O., Caillierez, R., Arrial, A., Bégard, S., Mortelecque, J., Eddarkaoui, S., Loyens, A., Cantrelle, F.-X., Hanoulle, X., Rain, J.-C., Colin, M., Buée, L., & Landrieu, I. (2022). Inhibition of Tau seeding by targeting Tau nucleation core within neurons with a single domain antibody fragment. *Molecular Therapy: The Journal of the American Society of Gene Therapy*, *30*(4), 1484–1499.

De Genst, E. J., Guilliams, T., Wellens, J., O'Day, E. M., Waudby, C. A., Meehan, S., Dumoulin, M., Hsu, S.-T. D., Cremades, N., Verschueren, K. H. G., Pardon, E., Wyns, L., Steyaert, J., Christodoulou, J., & Dobson, C. M. (2010). Structure and properties of a complex of α-synuclein and a single-domain camelid antibody. *Journal of Molecular Biology*, *402*(2), 326–343.

DeKosky, S. T., & Scheff, S. W. (1990). Synapse loss in frontal cortex biopsies in Alzheimer's disease: correlation with cognitive severity. *Annals of Neurology*, *27*(5), 457–464.

Denk, W., & Horstmann, H. (2004). Serial block-face scanning electron microscopy to reconstruct three-dimensional tissue nanostructure. *PLoS Biology*, *2*(11), e329.

Deszyński, P., Młokosiewicz, J., Volanakis, A., Jaszczyszyn, I., Castellana, N., Bonissone, S., Ganesan, R., & Krawczyk, K. (2021). INDI—integrated nanobody database for immunoinformatics. *Nucleic Acids Research*, *50*(D1), D1273–D1281.

Domínguez-Álvaro, M., Montero-Crespo, M., Blazquez-Llorca, L., Insausti, R., DeFelipe, J., & Alonso-Nanclares, L. (2018). Three-dimensional analysis of synapses in the transentorhinal cortex of Alzheimer's disease patients. *Acta Neuropathologica Communications*, *6*(1). https://doi.org/10.1186/s40478-018-0520-6

Fang, T., Lu, X., Berger, D., Gmeiner, C., Cho, J., Schalek, R., Ploegh, H., & Lichtman, J. (2018). Nanobody immunostaining for correlated light and electron microscopy with preservation of ultrastructure. *Nature Methods*, *15*(12), 1029–1032.

Ferrer, I., López-González, I., Carmona, M., Arregui, L., Dalfó, E., Torrejón-Escribano, B., Diehl, R., & Kovacs, G. G. (2014). Glial and neuronal tau pathology in tauopathies: characterization of disease-specific phenotypes and tau pathology progression. *Journal of Neuropathology and Experimental Neurology*, *73*(1), 81–97.

Fulton, K. A., & Briggman, K. L. (2021). Permeabilization-free en bloc immunohistochemistry for correlative microscopy. *ELife*, *10*. https://doi.org/10.7554/eLife.63392

Gouras, G. K., Tampellini, D., Takahashi, R. H., & Capetillo-Zarate, E. (2010). Intraneuronal beta-amyloid accumulation and synapse pathology in Alzheimer's disease. *Acta Neuropathologica*, *119*(5), 523–541.

Gowrishankar, S., Yuan, P., Wu, Y., Schrag, M., Paradise, S., Grutzendler, J., De Camilli, P., & Ferguson, S. M. (2015). Massive accumulation of luminal protease-deficient axonal lysosomes at Alzheimer's disease amyloid plaques. *Proceedings of the National Academy of Sciences of the United States of America*, *112*(28), E3699-708.

Habicht, G., Haupt, C., Friedrich, R. P., Hortschansky, P., Sachse, C., Meinhardt, J., Wieligmann, K., Gellermann, G. P., Brodhun, M., Götz, J., Halbhuber, K.-J., Röcken, C., Horn, U., & Fändrich, M. (2007). Directed selection of a conformational antibody domain that prevents mature amyloid fibril formation by stabilizing Abeta protofibrils. *Proceedings of the National Academy of Sciences of the United States of America*, *104*(49), 19232–19237.

Hampel, H., Hardy, J., Blennow, K., Chen, C., Perry, G., Kim, S. H., Villemagne, V. L., Aisen, P., Vendruscolo, M., Iwatsubo, T., Masters, C. L., Cho, M., Lannfelt, L., Cummings, J. L., & Vergallo, A. (2021). The Amyloid-β Pathway in Alzheimer's Disease. *Molecular Psychiatry*, *26*(10), 5481–5503.

Han, X., Lu, X., Li, P. H., Wang, S., Schalek, R., Meirovitch, Y., Lin, Z., Adhinarta, J., Berger, D., Wu, Y., Fang, T., Meral, E. S., Asraf, S., Ploegh, H., Pfister, H., Wei, D., Jain, V., Trimmer, J. S., & Lichtman, J. W. (2023). Multiplexed volumetric CLEM enabled by antibody derivatives provides

new insights into the cytology of the mouse cerebellar cortex. *BioRxiv.Org: The Preprint Server for Biology*. https://doi.org/10.1101/2023.05.20.540091

Harbaugh, R. E., Reeder, T. M., Senter, H. J., Knopman, D. S., Baskin, D. S., Pirozzolo, F., Chui, H. C., Shetter, A. G., Bakay, R. A., & Leblanc, R. (1989). Intracerebroventricular bethanechol chloride infusion in Alzheimer's disease. Results of a collaborative double-blind study. *Journal of Neurosurgery*, *71*(4), 481–486.

Hattori, R., Kuchibhotla, K. V., Froemke, R. C., & Komiyama, T. (2017). Functions and dysfunctions of neocortical inhibitory neuron subtypes. *Nature Neuroscience*, *20*(9), 1199–1208.

Hayat, M. A. (2000). *Principles and techniques of electron microscopy* (4th ed.). Cambridge University Press.

Hayworth, K. J., Kasthuri, N., Schalek, R., & Lichtman, J. W. (2006). Automating the Collection of Ultrathin Serial Sections for Large Volume TEM Reconstructions. *Microscopy and Microanalysis: The Official Journal of Microscopy Society of America, Microbeam Analysis Society, Microscopical Society of Canada*, *12*(S02), 86–87.

Hillman, D. E., & Chen, S. (1981). Plasticity of synaptic size with constancy of total synaptic contact area on Purkinje cells in the cerebellum. *Progress in Clinical and Biological Research*, *59A*, 229–245.

Im, K., Mareninov, S., Diaz, M. F. P., & Yong, W. H. (2019). An Introduction to Performing Immunofluorescence Staining. *Methods in Molecular Biology* , *1897*, 299–311.

Immunofluorescence Labeling of Free-Floating Perfusion-Fixed Brain Sections. (2016). NeuroMab. chrome-extension://efaidnbmnnnibpcajpcglclefindmkaj/https://neuromab.ucdavis.edu/files/NeuroMab%20brain%20IF%20protocol%200320.pdf

Januszewski, Michal, & Jain, V. (2019). Segmentation-Enhanced CycleGAN. In *bioRxiv*. bioRxiv. https://doi.org/10.1101/548081

Januszewski, Michał, Kornfeld, J., Li, P. H., Pope, A., Blakely, T., Lindsey, L., Maitin-Shepard, J., Tyka, M., Denk, W., & Jain, V. (2018). High-precision automated reconstruction of neurons with flood-filling networks. *Nature Methods*, *15*(8), 605–610.

Jiang, Y., Li, L., Pang, K., Liu, J., Chen, B., Yuan, J., Shen, L., Chen, X., Lu, B., & Han, H. (2022).

Synaptic degeneration in the prefrontal cortex of a rat AD model revealed by volume electron microscopy. *Journal of Molecular Cell Biology*, *14*(3). https://doi.org/10.1093/jmcb/mjac012

Johnson, E. C. B., Carter, E. K., Dammer, E. B., Duong, D. M., Gerasimov, E. S., Liu, Y., Liu, J., Betarbet, R., Ping, L., Yin, L., Serrano, G. E., Beach, T. G., Peng, J., De Jager, P. L., Haroutunian, V., Zhang, B., Gaiteri, C., Bennett, D. A., Gearing, M., … Seyfried, N. T. (2022). Large-scale deep multi-layer analysis of Alzheimer's disease brain reveals strong proteomic disease-related changes not observed at the RNA level. *Nature Neuroscience*, *25*(2), 213–225.

Johnson, E. C. B., Dammer, E. B., Duong, D. M., Ping, L., Zhou, M., Yin, L., Higginbotham, L. A., Guajardo, A., White, B., Troncoso, J. C., Thambisetty, M., Montine, T. J., Lee, E. B., Trojanowski, J. Q., Beach, T. G., Reiman, E. M., Haroutunian, V., Wang, M., Schadt, E., … Seyfried, N. T. (2020). Large-scale proteomic analysis of Alzheimer's disease brain and cerebrospinal fluid reveals early changes in energy metabolism associated with microglia and astrocyte activation. *Nature Medicine*, *26*(5), 769–780.

Kahlson, M. A., & Colodner, K. J. (2015). Glial Tau Pathology in Tauopathies: Functional Consequences. *Journal of Experimental Neuroscience*, *9*(Suppl 2), 43–50.

Karlupia, N., Schalek, R. L., Wu, Y., Meirovitch, Y., Wei, D., Charney, A. W., Kopell, B. H., & Lichtman, J. W. (2023). Immersion fixation and staining of multi-cubic millimeter volumes for electron microscopy-based connectomics of human brain biopsies. *Biological Psychiatry*. https://doi.org/10.1016/j.biopsych.2023.01.025

Kasthuri, N., Hayworth, K. J., Berger, D. R., Schalek, R. L., Conchello, J. A., Knowles-Barley, S., Lee, D., Vázquez-Reina, A., Kaynig, V., Jones, T. R., Roberts, M., Morgan, J. L., Tapia, J. C., Seung, H. S., Roncal, W. G., Vogelstein, J. T., Burns, R., Sussman, D. L., Priebe, C. E., … Lichtman, J. W. (2015). Saturated Reconstruction of a Volume of Neocortex. *Cell*, *162*(3), 648–661.

Kislinger, G., Gnägi, H., Kerschensteiner, M., Simons, M., Misgeld, T., & Schifferer, M. (2020). Multiscale ATUM-FIB Microscopy Enables Targeted Ultrastructural Analysis at Isotropic Resolution. *IScience*, *23*(7), 101290.

Knott, G., Marchman, H., Wall, D., & Lich, B. (2008). Serial Section Scanning Electron Microscopy of Adult Brain Tissue Using Focused Ion Beam Milling. In *Journal of Neuroscience* (Vol. 28, Issue

12, pp. 2959–2964). https://doi.org/10.1523/jneurosci.3189-07.2008

Koffie, R. M., Meyer-Luehmann, M., Hashimoto, T., Adams, K. W., Mielke, M. L., Garcia-Alloza, M., Micheva, K. D., Smith, S. J., Kim, M. L., Lee, V. M., Hyman, B. T., & Spires-Jones, T. L. (2009). Oligomeric amyloid β associates with postsynaptic densities and correlates with excitatory synapse loss near senile plaques. *Proceedings of the National Academy of Sciences*, *106*(10), 4012–4017.

Lafaye, P., Achour, I., England, P., Duyckaerts, C., & Rougeon, F. (2009). Single-domain antibodies recognize selectively small oligomeric forms of amyloid β, prevent Aβ-induced neurotoxicity and inhibit fibril formation. *Molecular Immunology*, *46*(4), 695–704.

Lafaye, P., Bay, S., Delatour, B., Dhenain, M., Duyckaerts, C., Li, T., Vandesquille, M., Czech, C., & Grueninger, F. (2019). Camelid single-domain antibody directed against amyloid bêta and methods for producing conjugates thereof (EPO Patent No. 3068799:B1). In *European Patent* (3068799:B1). https://patentimages.storage.googleapis.com/06/2d/dd/30cf8941c20327/EP3068799B1.pdf

Lafaye, P., Bay, S., Delatour, B., Dhenain, M., Duyckaerts, C., Li, T., Vandesquille, M., Czech, C., & Grueninger, F. (2020). Camelid single-domain antibody directed against phosphorylated tau proteins and methods for producing conjugates thereof (USPTO Patent No. 20200165329:A1). In *US Patent* (20200165329:A1). https://patentimages.storage.googleapis.com/88/2f/7a/dd7804c87c4ce3/US20200165329A1.pdf

LaFerla, F. M., Green, K. N., & Oddo, S. (2007). Intracellular amyloid-beta in Alzheimer's disease. *Nature Reviews. Neuroscience*, *8*(7), 499–509.

Lee, W.-C. A., Bonin, V., Reed, M., Graham, B. J., Hood, G., Glattfelder, K., & Reid, R. C. (2016). Anatomy and function of an excitatory network in the visual cortex. *Nature*, *532*(7599), 370–374.

Li, T., Vandesquille, M., Koukouli, F., Dudeffant, C., Youssef, I., Lenormand, P., Ganneau, C., Maskos, U., Czech, C., Grueninger, F., Duyckaerts, C., Dhenain, M., Bay, S., Delatour, B., & Lafaye, P. (2016). Camelid single-domain antibodies: A versatile tool for in vivo imaging of extracellular and intracellular brain targets. *Journal of Controlled Release: Official Journal of the Controlled Release Society*, *243*, 1–10.

Li, X., Kumar, Y., Zempel, H., Mandelkow, E.-M., Biernat, J., & Mandelkow, E. (2011). Novel diffusion barrier for axonal retention of Tau in neurons and its failure in neurodegeneration. *The EMBO Journal*, *30*(23), 4825–4837.

Lichtman, J. W., & Sanes, J. R. (2008). Ome sweet ome: what can the genome tell us about the connectome? *Current Opinion in Neurobiology*, *18*(3), 346–353.

Lin, Z., Wei, D., Lichtman, J., & Pfister, H. (2021). PyTorch Connectomics: A Scalable and Flexible Segmentation Framework for EM Connectomics. In *arXiv [eess.IV]*. arXiv. http://arxiv.org/abs/2112.05754

Loomba, S., Straehle, J., Gangadharan, V., Heike, N., Khalifa, A., Motta, A., Ju, N., Sievers, M., Gempt, J., Meyer, H. S., & Helmstaedter, M. (2022). Connectomic comparison of mouse and human cortex. *Science*, *377*(6602), eabo0924.

Lu, X., Han, X., Meirovitch, Y., Sjostedt, E., Schalek, R., & Lichtman, J. (2023). *Preserving extracellular space for high-quality optical and ultrastructural studies of whole mammalian brains*.

Lue, L.-F., Kuo, Y.-M., Roher, A. E., Brachova, L., Shen, Y., Sue, L., Beach, T., Kurth, J. H., Rydel, R. E., & Rogers, J. (1999). Soluble Amyloid β Peptide Concentration as a Predictor of Synaptic Change in Alzheimer's Disease. *The American Journal of Pathology*, *155*(3), 853–862.

Magistri, M., Velmeshev, D., Makhmutova, M., & Faghihi, M. A. (2015). Transcriptomics profiling of Alzheimer's disease reveal neurovascular defects, altered amyloid-β homeostasis, and deregulated expression of long noncoding RNAs. *Journal of Alzheimer's Disease: JAD*, *48*(3), 647–665.

Mandelkow, E. M., & Mandelkow, E. (1998). Tau in Alzheimer's disease. *Trends in Cell Biology*, *8*(11), 425–427.

Mathys, H., Davila-Velderrain, J., Peng, Z., Gao, F., Mohammadi, S., Young, J. Z., Menon, M., He, L., Abdurrob, F., Jiang, X., Martorell, A. J., Ransohoff, R. M., Hafler, B. P., Bennett, D. A., Kellis, M., & Tsai, L.-H. (2019). Single-cell transcriptomic analysis of Alzheimer's disease. *Nature*, *570*(7761), 332–337.

McMahon, C., Baier, A. S., Pascolutti, R., Wegrecki, M., Zheng, S., Ong, J. X., Erlandson, S. C., Hilger, D., Rasmussen, S. G. F., Ring, A. M., Manglik, A., & Kruse, A. C. (2018). Yeast surface display

platform for rapid discovery of conformationally selective nanobodies. *Nature Structural & Molecular Biology*, *25*(3), 289–296.

Meirovitch, Y., Mi, L., Saribekyan, H., Matveev, A., Rolnick, D., & Shavit, N. (2018). Cross-classification clustering: An efficient multi-object tracking technique for 3-D instance segmentation in connectomics. In *arXiv [cs.CV]* (pp. 8425–8435). arXiv. http://openaccess.thecvf.com/content_CVPR_2019/html/Meirovitch_Cross-Classification_Clustering_An_Efficient_Multi-Object_Tracking_Technique_for_3-D_Instance_CVPR_2019_paper.html

MICrONS Consortium, Alexander Bae, J., Baptiste, M., Bodor, A. L., Brittain, D., Buchanan, J., Bumbarger, D. J., Castro, M. A., Celii, B., Cobos, E., Collman, F., da Costa, N. M., Dorkenwald, S., Elabbady, L., Fahey, P. G., Fliss, T., Froudakis, E., Gager, J., Gamlin, C., … Yu, S.-C. (2021). Functional connectomics spanning multiple areas of mouse visual cortex. In *bioRxiv* (p. 2021.07.28.454025). https://doi.org/10.1101/2021.07.28.454025

Montero-Crespo, M., Domínguez-Álvaro, M., Alonso-Nanclares, L., DeFelipe, J., & Blazquez-Llorca, L. (2021). Three-dimensional analysis of synaptic organization in the hippocampal CA1 field in Alzheimer's disease. *Brain: A Journal of Neurology*, *144*(2), 553–573.

Mucke, L., Masliah, E., Yu, G.-Q., Mallory, M., Rockenstein, E. M., Tatsuno, G., Hu, K., Kholodenko, D., Johnson-Wood, K., & McConlogue, L. (2000). High-Level Neuronal Expression of Aβ1–42 in Wild-Type Human Amyloid Protein Precursor Transgenic Mice: Synaptotoxicity without Plaque Formation. *The Journal of Neuroscience: The Official Journal of the Society for Neuroscience*, *20*(11), 4050–4058.

Muyldermans, S. (2021). A guide to: generation and design of nanobodies. *The FEBS Journal*, *288*(7), 2084–2102.

Noble, W., Hanger, D. P., Miller, C. C. J., & Lovestone, S. (2013). The importance of tau phosphorylation for neurodegenerative diseases. *Frontiers in Neurology*, *4*, 83.

Oddo, S., Caccamo, A., Shepherd, J. D., Murphy, M. P., Golde, T. E., Kayed, R., Metherate, R., Mattson, M. P., Akbari, Y., & LaFerla, F. M. (2003). Triple-transgenic model of Alzheimer's disease with plaques and tangles: intracellular Abeta and synaptic dysfunction. *Neuron*, *39*(3), 409–421.

Pang, K., Jiang, R., Zhang, W., Yang, Z., Li, L.-L., Shimozawa, M., Tambaro, S., Mayer, J., Zhang, B., Li, M., Wang, J., Liu, H., Yang, A., Chen, X., Liu, J., Winblad, B., Han, H., Jiang, T., Wang, W., … Lu, B. (2022). An App knock-in rat model for Alzheimer's disease exhibiting Aβ and tau pathologies, neuronal death and cognitive impairments. *Cell Research*, *32*(2), 157–175.

Parag, T., Berger, D., Kamentsky, L., Staffler, B., Wei, D., Helmstaedter, M., Lichtman, J. W., & Pfister, H. (2019). Detecting synapse location and connectivity by signed proximity estimation and pruning with deep nets. In *Lecture Notes in Computer Science* (pp. 354–364). Springer International Publishing.

Pavarino, E. C., Yang, E., Dhanyasi, N., Wang, M. D., Bidel, F., Lu, X., Yang, F., Francisco Park, C., Bangalore Renuka, M., Drescher, B., Samuel, A. D. T., Hochner, B., Katz, P. S., Zhen, M., Lichtman, J. W., & Meirovitch, Y. (2023). mEMbrain: an interactive deep learning MATLAB tool for connectomic segmentation on commodity desktops. *Frontiers in Neural Circuits*, *17*, 952921.

Rajendran, L., & Paolicelli, R. C. (2018). Microglia-Mediated Synapse Loss in Alzheimer's Disease. *The Journal of Neuroscience: The Official Journal of the Society for Neuroscience*, *38*(12), 2911–2919.

Santurkar, S., Budden, D., Matveev, A., Berlin, H., Saribekyan, H., Meirovitch, Y., & Shavit, N. (2017). Toward Streaming Synapse Detection with Compositional ConvNets. In *arXiv [cs.CV]*. arXiv. http://arxiv.org/abs/1702.07386

Scheff, S. W., DeKosky, S. T., & Price, D. A. (1990). Quantitative assessment of cortical synaptic density in Alzheimer's disease. *Neurobiology of Aging*, *11*(1), 29–37.

Scheff, S. W., & Price, D. A. (1993). Synapse loss in the temporal lobe in Alzheimer's disease. *Annals of Neurology*, *33*(2), 190–199.

Scheff, Stephen W., & Price, D. A. (2006). Alzheimer's disease-related alterations in synaptic density: neocortex and hippocampus. *Journal of Alzheimer's Disease: JAD*, *9*(3 Suppl), 101–115.

Scheff, Stephen W., Price, D. A., Schmitt, F. A., & Mufson, E. J. (2006). Hippocampal synaptic loss in early Alzheimer's disease and mild cognitive impairment. *Neurobiology of Aging*, *27*(10), 1372–1384.

Scheffer, L. K., Xu, C. S., Januszewski, M., Lu, Z., Takemura, S.-Y., Hayworth, K. J., Huang, G. B.,

Shinomiya, K., Maitlin-Shepard, J., Berg, S., Clements, J., Hubbard, P. M., Katz, W. T., Umayam, L., Zhao, T., Ackerman, D., Blakely, T., Bogovic, J., Dolafi, T., … Plaza, S. M. (2020). A connectome and analysis of the adult Drosophila central brain. *ELife*, *9*. https://doi.org/10.7554/eLife.57443

Seo, J., Sim, Y., Kim, J., Kim, H., Cho, I., Nam, H., Yoon, Y.-G., & Chang, J.-B. (2022). PICASSO allows ultra-multiplexed fluorescence imaging of spatially overlapping proteins without reference spectra measurements. *Nature Communications*, *13*(1), 2475.

Shapson-Coe, A., Januszewski, M., Berger, D. R., Pope, A., Wu, Y., Blakely, T., Schalek, R. L., Li, P. H., Wang, S., Maitin-Shepard, J., Karlupia, N., Dorkenwald, S., Sjostedt, E., Leavitt, L., Lee, D., Bailey, L., Fitzmaurice, A., Kar, R., Field, B., … Lichtman, J. W. (2021). A connectomic study of a petascale fragment of human cerebral cortex. In *bioRxiv* (p. 2021.05.29.446289). https://doi.org/10.1101/2021.05.29.446289

Sobotzik, J.-M., Sie, J. M., Politi, C., Del Turco, D., Bennett, V., Deller, T., & Schultz, C. (2009). AnkyrinG is required to maintain axo-dendritic polarity in vivo. *Proceedings of the National Academy of Sciences of the United States of America*, *106*(41), 17564–17569.

Staffler, B., Berning, M., Boergens, K. M., Gour, A., Smagt, P. van der, & Helmstaedter, M. (2017). SynEM, automated synapse detection for connectomics. *ELife*, *6*. https://doi.org/10.7554/eLife.26414

Su, F., Wei, M., Sun, M., Jiang, L., Dong, Z., Wang, J., & Zhang, C. (2023). Deep learning-based synapse counting and synaptic ultrastructure analysis of electron microscopy images. *Journal of Neuroscience Methods*, *384*, 109750.

Taylor, J. P., Hardy, J., & Fischbeck, K. H. (2002). Toxic proteins in neurodegenerative disease. *Science*, *296*(5575), 1991–1995.

Turner, N. L., Macrina, T., Bae, J. A., Yang, R., Wilson, A. M., Schneider-Mizell, C., Lee, K., Lu, R., Wu, J., Bodor, A. L., Bleckert, A. A., Brittain, D., Froudarakis, E., Dorkenwald, S., Collman, F., Kemnitz, N., Ih, D., Silversmith, W. M., Zung, J., … Seung, H. S. (2022). Reconstruction of neocortex: Organelles, compartments, cells, circuits, and activity. *Cell*, *185*(6), 1082-1100.e24.

Twohig, D., & Nielsen, H. M. (2019). α-synuclein in the pathophysiology of Alzheimer's disease. *Molecular*

Neurodegeneration, *14*(1), 23.

Uchida, Y., & Takahashi, H. (2008). Rapid detection of Abeta deposits in APP transgenic mice by Hoechst 33342. *Neuroscience Letters*, *448*(3), 279–281.

Urbanc, B., Cruz, L., Le, R., Sanders, J., Ashe, K. H., Duff, K., Stanley, H. E., Irizarry, M. C., & Hyman, B. T. (2002). Neurotoxic effects of thioflavin S-positive amyloid deposits in transgenic mice and Alzheimer's disease. *Proceedings of the National Academy of Sciences of the United States of America*, *99*(22), 13990–13995.

Vilalta, A., & Brown, G. C. (2018). Neurophagy, the phagocytosis of live neurons and synapses by glia, contributes to brain development and disease. *The FEBS Journal*, *285*(19), 3566–3575.

Volpi, E. V., & Bridger, J. M. (2008). FISH glossary: an overview of the fluorescence in situ hybridization technique. *BioTechniques*, *45*(4), 385–386, 388, 390 passim.

Wei, L., Chen, Z., Shi, L., Long, R., Anzalone, A. V., Zhang, L., Hu, F., Yuste, R., Cornish, V. W., & Min, W. (2017). Super-multiplex vibrational imaging. *Nature*, *544*(7651), 465–470.

Wilson, A. C., Dugger, B. N., Dickson, D. W., & Wang, D.-S. (2011). TDP-43 in aging and Alzheimer's disease - a review. *International Journal of Clinical and Experimental Pathology*, *4*(2), 147–155.

Wilton, E. E., Opyr, M. P., Kailasam, S., Kothe, R. F., & Wieden, H.-J. (2018). sdAb-DB: The Single Domain Antibody Database. *ACS Synthetic Biology*, *7*(11), 2480–2484.

Yu, M., Sporns, O., & Saykin, A. J. (2021). The human connectome in Alzheimer disease - relationship to biomarkers and genetics. *Nature Reviews. Neurology*, *17*(9), 545–563.

Zempel, H., Dennissen, F. J. A., Kumar, Y., Luedtke, J., Biernat, J., Mandelkow, E.-M., & Mandelkow, E. (2017). Axodendritic sorting and pathological missorting of Tau are isoform-specific and determined by axon initial segment architecture. *The Journal of Biological Chemistry*, *292*(29), 12192–12207.

Zimmermann, I., Egloff, P., Hutter, C. A. J., Kuhn, B. T., Bräuer, P., Newstead, S., Dawson, R. J. P., Geertsma, E. R., & Seeger, M. A. (2020). Generation of synthetic nanobodies against delicate proteins. *Nature Protocols*, *15*(5), 1707–1741.

Zuiderveld, K. (1994). Contrast limited adaptive histogram equalization. *Graphics Gems*, *0*, 474–485.